Pediatric Thoracic MRI

21

Mark C. Liszewski, Pierluigi Ciet, Giuseppe Cicero, and Edward Y. Lee

Introduction

MRI of the pediatric thorax has historically been constrained by technical factors including artifact from respiratory and cardiac motion, rapid signal dephasing at air-tissue interfases, and relatively low proton density within the lung. Advances in MRI scanner technology have made it possible to overcome many of these constraints. The current generation of MRI scanners available in most imaging centers is capable of performing imaging studies of diagnostic quality to evaluate many conditions of the pediatric thorax. In this chapter, MR imaging techniques for imaging the pediatric chest are presented. The MR imaging findings in a spectrum of anomalies and abnormalities of the pediatric chest are then presented and illustrated.

Imaging Techniques

The main advantage of chest MRI is its ability of integrating excellent anatomical as well as physiologic information under a single examination. Nonetheless, chest MRI faces many challenges.

M. C. Liszewski
Department of Radiology, Division of Pediatric Radiology, Montefiore Medical Center, Bronx, NY, USA

P. Ciet
Department of Radiology and Nuclear Medicine, Sophia Children Hospital – Erasmus Medical Center, Rotterdam, The Netherlands

G. Cicero
Department of Radiology and Nuclear Medicine, Sophia Children Hospital – Erasmus Medical Center, Rotterdam, The Netherlands

Department of Biomedical Sciences and Morphological and Functional Imaging, University of Messina, Messina, Italy

E. Y. Lee (✉)
Department of Radiology, Boston Children's Hospital and Harvard Medical School, Boston, MA, USA
e-mail: Edward.Lee@childrens.harvard.edu

Signal-to-Noise Ratio (SNR) in Chest MRI

The lung parenchyma is an organ with a relatively small number of water protons and high content of air. These two conditions result in intrinsically low signal on chest MRI.

Due to the low proton content of the healthy lung parenchyma, the voxel size in chest MRI is usually adjusted to be significantly larger than that of CT in order to maximize signal. The slice thickness achieved with chest MRI protocols generally range between 3 and 5 mm, which is 3–5 times thicker than that of CT. However, the newest ultrashort (UTE) and zero echo time (ZTE) MRI readout schemes provide higher SNR with thinner slices enabling submillimeter isotropic resolution [1]. These acquisition schemes are usually acquired in free-breathing conditions with respiratory triggering and a long acquisition time. However, breath-hold acquisition can be obtained by using parallel imaging [2]. With parallel imaging techniques, the spatial information related to each phased array coil element is utilized for reducing the amount of conventional encoding lines in order to gain spatial or temporal resolution [2]. The higher parallel imaging factor or "acceleration" utilized, the higher the penalty in SNR due to a higher noise. The most appropriate parallel imaging techniques for chest MRI are those that reconstruct the image in the frequency domain, before the Fourier transform, from the frequency signals of each coil such as in the case of GRAPPA (GeneRalized Autocalibrating Partially Parallel Acquisition) or ARC (Autocalibrating Reconstruction for Cartesian imaging) [2]. Using GRAPPA or ARC, comfortable breath-hold acquisition can be achieved (6–15 s), which can be easily performed in children older than 5 years.

Signal loss in chest MRI is directly related to the T2 star (T2∗) effect of air-tissue interfaces, which are particularly strong with gradient recalled echo (GRE) techniques. When using GRE sequences, the shortest TE achievable should be employed to ensure optimal SNR. This can be obtained with MR scanners that have powerful slew rate of 200 T/m/ms or more. Independent of the sequence used, imaging at

R. H. Cleveland, E. Y. Lee (eds.), *Imaging in Pediatric Pulmonology*, https://doi.org/10.1007/978-3-030-23979-4_21

end-inspiration provides lower SNR than scanning performed at end-expiration due to the larger amount of air within the lung.

Breathing and Cardiac Motion Compensation

Image quality in chest MRI is influenced by cardiac and breathing motion, which determines SNR dephasing. This problem is more severe in children, who have higher respiratory and cardiac rates than adults. To eliminate these motion effects, image acquisition can be synchronized with the motion itself (respiratory or ECG gating), or data can be averaged over many respiratory cycles without any specific form of synchronization. Respiratory and cardiac triggering are performed using navigator echoes or cardiac and respiratory monitoring devices, such as pneumobelts and ECG leads. Navigator echo techniques detect the diaphragm position in real time and trigger the image acquisition prospectively, most often selecting the diaphragm position at end-expiration. Navigator echo-based techniques improve image quality, but this is at the expense of longer acquisition times, especially in patients with irregular breathing patterns [2]. Pneumobelts are external devices placed around the rib cage, which monitor chest excursion and trigger image acquisition at end-expiration. Multiple averaging techniques are used during free breathing to reduce image ghosting. An advantage of this technique over techniques using respiratory and cardiac triggering is constant scan times. A drawback of this technique is image blurring. Some or all of these motion compensation techniques are routinely employed when imaging children under 5 years of age, who cannot follow breathing instructions.

Patient Preparation

Children younger than 5 years of age are usually scanned under moderate sedation or total anesthesia in combination with free-breathing MRI techniques. For infants, many pediatric centers use the "feed and wrap" method, where the child is fed immediately before the MRI scan and placed in the gantry after being swaddled [3].

Children older than 5 years can be coached to perform specific breathing maneuvers before or during the MRI scan. This coaching is crucial in children, who are less capable to follow instructions than adults. The training can be performed in a mock MRI scanner, which reproduces the noisy environment of a true MRI system and acquaints the child with the MRI setting. Depending on the examination performed, the patients are asked to maintain a breath-hold at inspiration or expiration, to breathe regularly, or to perform rapid expiratory and inspiratory or coughing maneuvers in order to study the response of the airways to stress situations.

MRI Protocols

Selection of an appropriate chest MRI protocol requires one to consider several factors including the type of contrast needed, SNR, contrast-to-noise ratio (CNR), and spatial and temporal resolution. Two groups of sequences can be used for chest MRI: spin echo (SE) or gradient echo (GRE). These sequences may collect imaging data during breath-hold conditions using ultrafast bidimensional (2D) and three-dimensional (3D) MR pulse sequences, which are usually preferred for chest MRI and MR angiography (MRA). These sequences freeze respiratory and/or cardiac motion allowing short acquisition times, which are indispensable in pediatric patients, who are not capable of long apnea times. In the group of 2D SE, several single-shot turbo SE (TSE) sequences are used. A typical 2D T2-weighted single-shot TSE scan is the Half-Fourier-Acquired Single-shot Turbo spin Echo (HASTE; RARE or SSFSE depending on the MRI scan manufacturer). One particular TSE non-breath-hold readout is the Periodically Rotated Overlapping ParallEL Lines with Enhanced Reconstruction (PROPELLER) sequence, which collects imaging data using rotating k-space bands or blades and is relatively insensitive to respiratory movement [4]. This sequence is more suitable for patients who are unable to comply with breathing instructions, such as children. TSE techniques have high sensitivity and SNR for fluid detection, evaluation of nodules, consolidation, and bronchial wall thickening [2].

2D or 3D GRE acquisitions include spoiled RF GRE readouts (SPGR, FLASH) or steady-state free precession SSFP readouts (trueFISP, FIESTA). Both of these sequences allow for high SNR and CNR in young noncooperative children. Short and ultrashort TE GRE scans are usually collected with very short TRs when compared to TSE scans, which is important for children who can only hold their breaths for a short time. 3D GRE acquisitions are more advantageous than the 2D scans, because they provide better SNR and are less sensitive to susceptibility artifacts than 2D scans [2]. In general, 3D GRE acquisitions can scan the entire thorax with isotropic voxels of 2–3 mm in less than 15 seconds. Isotropic voxels enable multiplanar reformats (MPR) which are important in the evaluation of vascular and airway structures. FLASH/SPGR sequence can be proton density weighted, which is most helpful for evaluating the lung parenchyma, vascular structures, and airways without the use of contrast agents (using a low flip angle) or T1-weighted, which is most helpful for MRA studies. SSFP/

TruFISP sequences generate a T1-/T2-weighted contrast with medium to high flip angle settings enhancing tissues in the lung with more water-like behavior, such as mucus plugs in the airways. SSFP has been used to assess relevant structural abnormalities, such as bronchiectasis, mucus plugging, and consolidation.

Functional Imaging

MRI has several techniques that can be used to assess multiple functional aspects of the lung and airways. Contrast-enhanced MRI has been used in pulmonary vasculature assessment and lung perfusion [2]. Cine-MRI has proven to be useful to assess central airway mechanics [5, 6]. Diffusion-weighted imaging (DWI) has been used to assess lung inflammation [7]. Fourier decomposition (FD) can be used to assess lung perfusion and lung ventilation without the use of contrast media [8].

Magnetic Resonance Angiography (MRA)

Magnetic resonance angiography (MRA) of the chest can be obtained without and with intravenous contrast agents [2]. The noncontrast studies are based on SSFP sequences ("bright blood") and SSFSE/HASTE sequences ("black blood"). The sequences are particularly advantageous in children, because they do not require the use of gadolinium. Therefore, these techniques can be repeated numerous times without concern about gadolinium deposition, which has been recently raised as a concern [9]. SSFSE dark blood sequences are usually applied to study the anatomy of the heart, great vessels, and mediastinum.

Contrast-enhanced MRI (CEMRI) provides higher temporal and spatial resolution than noncontrast-enhanced techniques [2]. CEMRI uses high temporal resolution 2D/3D T1-weighted GRE imaging and an acquisition rate of one image every 1.0–1.5 s with short TR (3–5 ms), short TE (1–2.5 ms), flip angle >15–60°, and resolution and coverage adjusted to breath-hold. For safety reasons, macrocyclic non-ionic agents (Gd-HP-DO3A [Dotarem] or Gd-BT-DO3A [Gadovist]) are preferred in pediatric patients, with doses ranging between 1 and 2 ml/kg and injection rates of up to 2 ml/sec [2]. In pediatric patients, CEMRI is used to study congenital vascular anomalies.

Perfusion MR Imaging

Perfusion defects can be assessed on MRI by administering contrast and performing dynamic contrast-enhanced (DCE) imaging or with FD [2]. DCE is obtained by fast imaging of the first pass of contrast agent through the lungs after intravenous bolus injection. 3D GRE sequences with high spatial and temporal resolution (e.g., FLASH, TREAT, TWIST, and TRICKS) are used.

FD is a recent technique that supplies perfusion and ventilation maps without intravenous or gaseous contrast agents. FD is based on a 2D SSFP/SPGR sequence with high temporal resolution without cardiac or respiratory gating. After data collection, image registration techniques are applied to compensate for respiratory motion. Fourier transform is eventually used to decompose the signal intensity changes of the lung parenchyma related to the cardiac and respiratory cycle and to obtain the perfusion- and ventilation-weighted images. Upgraded versions of the post-processing software for FD have shown an improvement of SNR and image quality [10], making this technique superior to nuclear medicine studies to assess ventilation/perfusion defects. This technique has been tested in patients with cystic fibrosis, chronic pulmonary embolism, and COPD [11].

Cine MR Imaging

Cine-MRI allows evaluation of the lung in dynamic conditions. Fast temporal resolution techniques, such as 3D GRE FLASH, have been used to delineate the diaphragmatic domes and chest wall during active breathing. Campbell et al. has proposed cine-MRI to assess and monitor pediatric patients after spinal surgery for scoliosis [12]. 2D SSFP multiphase or 3D TRICKS can be used to assess airways in dynamic conditions. Typical breathing maneuvers are forced expiration or coughing, which are used to reproduce the breathing condition occurring during exercise. Ciet et al. used a cine-MRI protocol to assess tracheobronchomalacia (TBM) in a group of pediatric patients and in a cohort of adult with saber-sheath TBM [5, 6].

In short, chest MRI, by combining functional and structural information, can be a powerful tool in pediatric thoracic imaging by providing information about ventilation, inflammation, perfusion, and structure (VIPS-MRI) [13]. A summary of VIPS-MRI protocol is presented in Table 21.1.

Spectrum of Thoracic Anomalies and Abnormalities

Since MRI and CT are both cross-sectional imaging modalities, the basic MR imaging findings in disorders of the pediatric chest are similar to the findings on CT. A practitioner familiar with CT of the pediatric chest should have little difficulty identifying the same pathology on MRI. In addition, MRI often provides the opportunity to obtain more information than CT. Because MRI does not involve the use of ionizing radiation, multiple MRI sequences with different tissue weighting, multiphase contrast-enhanced imaging, and

Table 21.1 Imaging protocols for ventilation, inflammation, perfusion, and structural (VIPS) MRI (lung, static airway, and dynamic airway)

Sequence	Manufacturer acronyms	Typical contrast	Average acquisition time (for entire chest, otherwise stated)	Spatial resolution/scan plane	Temporal resolution	Scan parameters	Field strength
Ventilation							
2D steady-state free precession gradient echo – SSFP	**FIESTA** (GE) **TruFISP** (SIEMENS) **Balanced FFE** (PHILIPS)	T1-/T2-weighted Inflow enhancement Bright blood	3–9 minutes Free-breathing	FOV = 450 × 450 mm SL =12 mm Matrix = 128 × 128 coronal or sagittal	3–4 images/s	TR = shortest (1.8–2.2 ms) TE = shortest (0.7–0.9 ms) FA = 65° BW = medium – high	1.5 T
2D RF-spoiled gradient echo	**SPGR** (GE) **FLASH** (SIEMENS) **FFE** (PHILIPS)	T1-weighted Inflow enhancement Bright blood	3–9 minutes Free-breathing	FOV = 500 × 500 mm SL = 15 mm Matrix = 256 × 192 coronal or sagittal	3–4 images/s	TR = shortest (1.8–2.2 ms) TE = shortest (0.7–0.9 ms) FA = low (<5°) BW = medium – high	1.5 T and 3.0 T
Inflammation							
2D single-shot echo-planar imaging sequence (EPI)	**EPI – DWI** (GE,SIEMENS, PHILIPS)	T2-weighted Diffusion weighted Black blood	5–7 minutes Free-breathing	FOV = 420 × 210 mm SL = 6 mm Matrix = 100 × 128 Axial	Low	TR = long (>4000 ms) TE = medium – long (>60 ms) FA = 90°/180° b = 0 and 600 s/mm^2 BW = high Fat suppressed	1.5 T and 3.0 T
2D single-shot echo-planar imaging (EPI) sequence	**EPI – DWI** (GE,SIEMENS, PHILIPS)	T2-weighted Perfusion and diffusion weighted Black blood	5–7 minutes Free-breathing	FOV = 420 × 210 mm SL = 6 mm Axial	Low	TR = long (>4000 ms) TE = medium – long (>60 ms) FA = 90°/180° b = 0, 10, 20, 30, 50, 70, 100, 150, 200, 400, 800 s/mm^2 BW = high Fat suppressed	1.5 T and 3.0 T
2D fast spin echo	**FSE** (GE) **TSE** (SIEMENS) **TSE** (PHILIPS)	T2-weighted Black blood	5–7 minutes Free-breathing	FOV = 400 mm SL = 5–7 mm Matrix = 256 × 192 axial and coronal	Low	TR = long (2000–4000 ms) TE = medium – long (>60 ms) FA = 90°/110° – 160° BW = low – medium Fat suppression	1.5 T and 3.0 T
Perfusion/angiography							
2D steady-state free precession gradient echo – SSFP	**FIESTA** (GE) **TruFISP** (SIEMENS) **balanced FFE** (PHILIPS)	See scan parameters above					
2D RF-spoiled gradient echo	**SPGR** (GE) **FLASH** (SIEMENS) **FFE** (PHILIPS)	See scan parameters above					
3D RF-spoiled gradient echo	**SPGR** (GE) **FLASH** (SIEMENS) **FFE** (PHILIPS)	T1-weighted, after contrast injection Bright blood	12–20 seconds End-expiratory breath-hold, shallow breathing	FOV = 460 mm Matrix = 40 × 192 × 256 Voxel size (<8 mm^3) sagittal or coronal	Low	TR = short (2.5–3 ms) TE = short (1.0–1.5 ms) FA = 30–40° BW = medium – high	1.5 T and 3.0 T

3D RF spoiled gradient echo	**TRICKS** (GE) **TWIST** (SIEMENS) **TRACK** (PHILIPS)	T1-weighted, after contrast injection k-space shared acquisition Bright blood	Breath-hold (end-expiratory)/ shallow breathing	FOV = 460 mm Matrix = 32 × 96 × 128 Voxel size (<12 mm^3) sagittal or coronal	Medium, 0.5–1 s/ volume	TR = short (2.0–2.5 ms) TE = shortest (0.8–1.1 ms) FA = 8–20° BW = medium – high	1.5 T and 3.0 T
Structure (including static airways)							
2D fast spin echo	**PROPELLER** (GE) **BLADE** (SIEMENS) **MultiVane** (PHILIPS)	T2-weighted Black blood	End-expiratory with navigator echo triggering 3–7 minutes according respiratory pace and pattern	FOV = 380–400 mmMatrix = 200 × 200 SL = 5–6 mm axial and coronal	Low	TR = respiratory rate (2–5 seconds) TE = short – medium (25–60 ms) FA = 90°/150° ± FAT Saturation BW = low – medium	1.5 T and 3.0 T
2D SSFP	**FIESTA** (GE) **TRUFISP** (SIEMENS) **Balanced FFE** (PHILIPS)	T1-/T2-weighted Bright blood	12–20 seconds Breath-hold	FOV = 400 mmMatrix = 160 × 160 SL = 2.5–5 mm axial and coronal	High	TR = shortest (<4 ms) TE = shortest (<2 ms) FA = 40° BW = high	1.5 T
3D fast spin echo	**CUBE** (GE) **SPACE** (SIEMENS) **VISTA** (PHILIPS)	T2-weighted Black blood	End-expiratory with pencil-beam navigator triggering 5–7 min	FOV = 320 mmMatrix = 160 × 160SL = 2 mm sagittal or coronal	Low	TR = respiratory rate (2–5 seconds)TE = medium (60 ms~) FA = 90°/variable flip train BW = medium – high Echo train length = 80–140 Fat saturation	1.5 T and 3.0 T
3D RF-spoiled gradient echo	**SPGR** (GE) **VIBE** (SIEMENS) **THRIVE** (PHILIPS)	PD- to T1-weighted	Breath-hold 10–12 seconds (inspiratory and expiratory)	FOV = 400 mmMatrix = 200 × 200 SL = 2 mm Isotropic voxel, as low as 8 mm^3 sagittal or coronal	High	TR = shortest (<1.7 ms) TE = shortest (<0.7 ms) FA = 2° BW = medium – high	1.5 T and 3.0 T
3D RF-spoiled gradient echo	**STARVIBE** (SIEMENS) clinically not available for GE or PHILIPS	PD- to T1-weighted	Free-breathing3–5 min	FOV = 400 mm Matrix = 320 × 320 SL = 1.2–4 mm voxel (2–5 mm^3) axial	Low	TR = 7.46 ms TE = 2.46 ms FA = 9° BW = medium	1.5 T and 3.0 T
3D 2-point Dixon RF-spoiled gradient echo	**LAVA FLEX** (GE)	PD to T1-weighted Water-only, fat-only, in-phase and out-of-phase contrast	Breath-hold (10s) Free-breathing (pencil-beam navigator)	FOV = 260 mm Matrix = 128 × 128 SL = 3 mm Voxel (<3 mm^3) axial	High	TR = 3.7–4.5 ms TE = min full (<2.0 ms) FA = 2–10° BW = medium – high	1.5 T and 3.0 T
3D ultrashort TE gradient echo	**UTE/VNAV(GE)** **PETRA/ SPIRALVIBE (SIEMENS)** **MultiVane** (PHILIPS)	PD-weighted, slight T1-weighting depending on readout flip angle chosen UTE	7–10 min Free-breathing	FOV = 360 mmvoxel size = 1–8 mm^3 Sagittal or coronal	Low	TR = short (<5 ms) TE = 0.07 msBW = medium – high	1.5 T and 3.0 T

(continued)

Table 21.1 (continued)

Sequence	Manufacturer acronyms	Typical contrast	Average acquisition time (for entire chest, otherwise stated)	Spatial resolution/scan plane	Temporal resolution	Scan parameters	Field strength
3D ultrashort TE gradient echo	**ZTE** (GE)	PD-weighted Slight T1-weighting depending on readout flip angle chosen **Silent**	7–10 min Free-breathing	FOV = 360 mmMatrix = 360 × 360 × 360 sagittal or coronal	Low	TR = shortest (<1.3 ms) TE = 0 ms BW = medium – High	1.5 T and 3.0 T
Dynamic airways							
2D steady-state free precession gradient echo – SSFP	**FIESTA** (GE)**TruFISP** (SIEMENS) **balanced FFE** (PHILIPS)	T1-/T2-weighted Inflow enhancement	3–4 minutes Hyperventilation Coverage larynx to carina ~ 4 seconds per slice position	FOV = 450 × 160 mm SL = 8 mm Matrix = 128 × 128 axial	4–5 images/s	TR = shortest (1.8 ms – 2.4 ms) TE = shortest (<1.2 ms) FA = 35° BW = medium – high	1.5 T
3D RF-spoiled gradient echo	**TRICKS** (GE) **TWIST** (SIEMENS) **4D TRACK** (PHILIPS)	PD- to T1-weighted	20 seconds Forced expiration, free-breathing or hyperventilation	FOV = 300 mm Matrix = 80 × 100 SL = 3.2 mm sagittal	<400 ms/ volume	TR = shortest (<2 ms) TE = minimum (<1.1 ms) FA = 2° BW = medium – high	1.5 T and 3.0 T

Reprinted from pending MRI Clinics Article, permission pending

dynamic imaging are routinely performed in MRI of the chest. This often allows MRI to provide greater information about tissue composition than CT. MR imaging findings in the spectrum of anomalies and abnormalities of the pediatric chest are presented and illustrated in the following section.

Vascular Thoracic Anomalies and Abnormalities

In children, echocardiography is often the first imaging modality used to evaluate mediastinal vascular anomalies, as it is often able to provide diagnostic images without the use of ionizing radiation or intravenous contrast [14]. Cross-sectional imaging with MRI or CT is often indicated to further characterize lesions first detected on echocardiography [15]. MRI has a well-established role in the evaluation of mediastinal vascular anomalies and abnormalities in children. MRA is typically able to provide excellent depiction of the mediastinal vasculature and provide necessary information for diagnosis and surgical planning. In many centers, contrast-enhanced MRI with MRA has replaced contrast-enhanced CT angiography for this indication. Although MRI has the advantage of not requiring ionizing radiation, MRI requires longer acquisition times compared to CT and is more susceptible to motion artifact. Therefore sedation or anesthesia is often needed to perform MRI in pediatric patients. In this scenario, the risks of ionizing radiation must be balanced with the risks of sedation when choosing between CT and MRI.

MR imaging findings of several commonly encountered mediastinal vascular anomalies and abnormalities associated with congenial lung malformations are illustrated in the following sections.

Obstructive Lesions

Interrupted Aortic Arch

Interrupted aortic arch (IAA) is a congenital condition defined by discontinuity between the ascending and descending thoracic aorta. IAA is rare, occurring in approximately 2 per 100,000 live births [15]. IAA is classified into type A (arch interruption is distal to the origin of the left subclavian artery), type B (arch interruption is between the origins of the left common carotid and left subclavian arteries), and type C (arch interruption is between the origins of the brachiocephalic and left common carotid arteries). In a review of 95 cases by Schreiber et al., 13% were type A, 84% were type B, and 3% were type C [16]. The right subclavian artery may arise normally (subtype 1), distal to left subclavian artery (subtype 2), or from a right ductus arteriosus (subtype 3). IAA is often associated with other congenital cardiac lesions, most commonly ventriculoseptal defect (VSD), patent ductus arteriosus and truncus arteriosus, and specific associations vary depending on the type of IAA [15]. IAA typically causes symptoms soon after birth with heart failure or shock, which typically worsens with closure of the ductus arteriosus [15, 17]. Initial treatment is with IV prostaglandin to maintain patency of the ductus arteriosus, followed by surgical correction in the first few days of life [15, 17].

Imaging evaluation of IAA is essential to surgical planning. Traditionally, this was achieved with a combination of echocardiography and catheter angiography [17]. However echocardiography can sometimes be limited in the evaluation of the aorta, and catheter angiography is invasive; therefore CTA and MRA may be utilized [17, 18]. MRA may be preferable to CTA given the lack of associated ionizing radiation, although MRA does often require sedation or anesthesia. The characteristic imaging finding of IAA on MRI is nonvisualization of a portion of the aortic arch [17]. This is typically well visualized on both unenhanced and contrast-enhanced MRA sequences.

Coarctation of Aorta

Aortic coarctation is characterized by focal narrowing of the aorta in the region of the aortic isthmus, defined as the portion of the aorta between the origin of the left subclavian artery and the ductus arteriosus [15]. Coarctation of the aorta is relatively common, occurring in approximately 4 of 10,000 live births [19]. Aortic coarctation may be associated with other congenital heart defects, most commonly VSD and bicuspid aortic valve [15, 20]. Within the first few months of life, collateral arteries begin to form between the proximal and distal aorta in order to allow blood flow to bypass the aortic narrowing [15]. Clinical presentation is usually during infancy, with heart murmur, decreased femoral pulses, and supine arm-leg blood pressure gradient of greater than 20 mmHg [21]. Early diagnosis and treatment is important to reduce development of long-term sequelae. Surgical treatment is preferred in infants and young children, and percutaneous transcatheter treatment is preferred in older patients [21].

The primary imaging modality used for initial diagnosis of aortic coarctation in the newborn and infant is echocardiography [14]. However, poor sonographic windows to this region often limit complete evaluation and advanced imaging with CT or MRI are routinely utilized for further characterization and surgical planning. CTA offers the advantage of excellent temporal resolution but requires ionizing radiation and is not able to provide hemodynamic information [21]. Therefore, MRI with three-dimensional contrast-enhanced MRA is often the preferred cross-sectional imaging modality for evaluation of aortic coarctation. The primary imaging finding in aortic coarctation on MRA is focal narrowing of the aorta in the region of the aortic isthmus (Fig. 21.1). In addition, large collateral vessels are often visible on

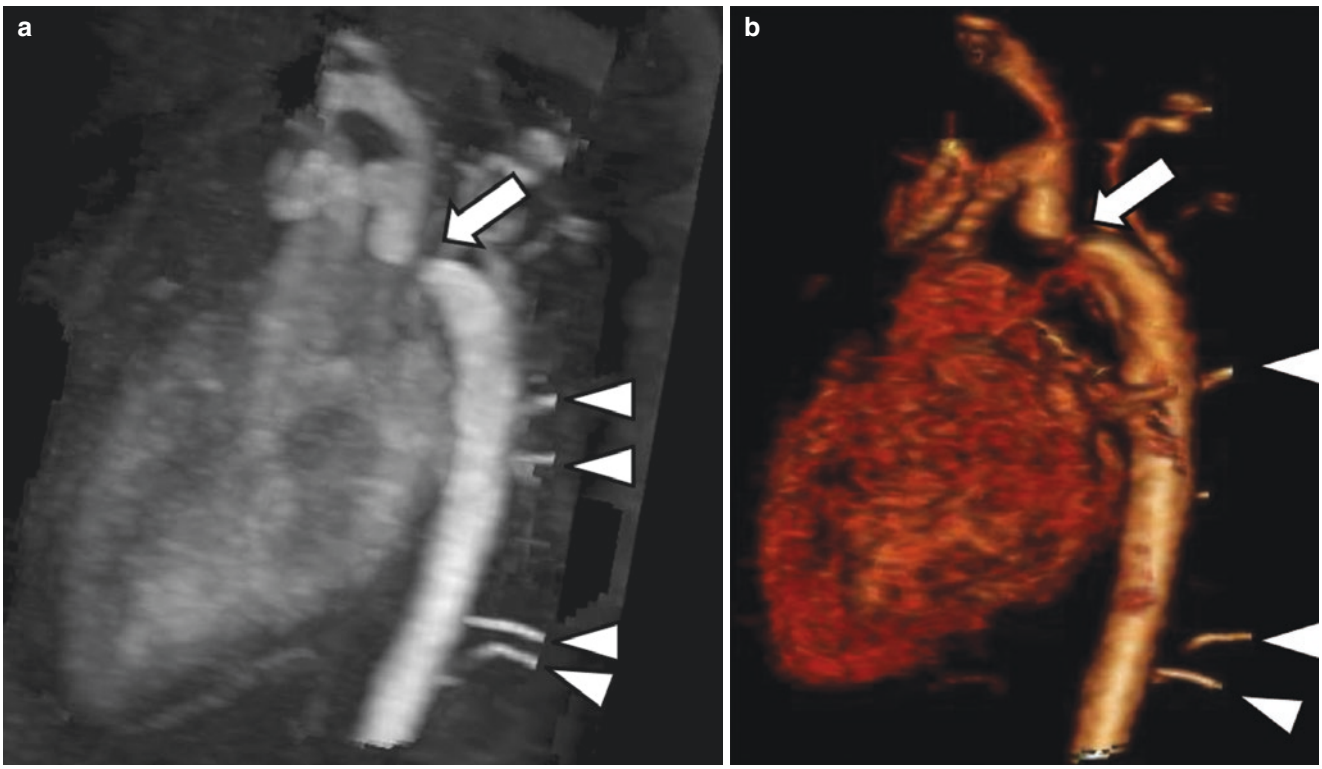

Fig. 21.1 A 2-year-old girl with aortic coarctation. (**a**) Maximum intensity projection image from enhanced T1-weighted MR angiogram with fat suppression shows narrowing (arrow) of the aortic isthmus and multiple collateral arteries (arrowheads) arising from the descending thoracic aorta. (**b**) 3D volume-rendered image from enhanced T1-weighted MR angiogram with fat suppression shows narrowing of the aortic isthmus (arrow) and multiple collateral arteries (arrowheads) arising from the descending thoracic aorta

MRA. Phase-contrast sequences can be used to estimate the pressure gradient across the coarctation and quantify collateral flow [21]. Given the lack of ionizing radiation, MRI is ideal for follow-up imaging. Long-term complications which may be seen on follow-up MRI include recoarctation, aneurysm, and dissection [21].

Vascular Rings and Sling

Double Aortic Arch

Double aortic arch occurs during embryonic development when the right arch does not regress and both the right and left arches persist [15]. The result is two aortic arches that encircle the trachea and esophagus, causing a vascular ring [15]. Signs and symptoms of double aortic arch are primarily due to mass effect on the trachea and esophagus. Compression of the trachea may cause wheezing, stridor, and tachypnea, and compression of the esophagus may cause dysphagia [22]. The aortic arches are often asymmetric in size. Dominant right arch with small left arch is most common (80%), while dominant left arch (10%) and balanced aortic arches (10%) are less common [23]. Preoperative imaging assessment is essential, as the smaller arch is typically resected [22, 24].

The imaging evaluation of double aortic arch often begins with echocardiography, which may depict the double arch and also evaluates for associated congenital heart disease, which is present in 12% of cases [22, 23]. Definition of the precise anatomy of double aortic arch is highly important for surgical planning, and advanced imaging with contrast-enhanced CTA or MRA is essential. Both CT and MRI have similar performance when depicting the double aortic arch [25]. MRI can often be successfully performed without sedation or anesthesia in infants, utilizing a "feed and swaddle" technique, and when possible MRI is preferred given the lack of ionizing radiation [26]. When the "feed and swaddle" technique is not successful, the risks of ionizing radiation with CT must be weighed against the risks of sedation and anesthesia with MRI. Imaging findings of double aortic arch include right and left aortic arches which both arise from the ascending aorta, encircle the trachea and esophagus, and then join to form a single descending thoracic aorta [15, 24] (Fig. 21.2). It is particularly important to define the arch anatomy in each case, identifying the smaller arch or depicting the balanced arch to aid in surgical planning and define which aortic arch to resect [22].

Right Aortic Arch with an Aberrant Left Subclavian Artery

Right aortic arch with an aberrant left subclavian artery is the most common type of right aortic arch and the second most common type of vascular ring after double aortic arch [15].

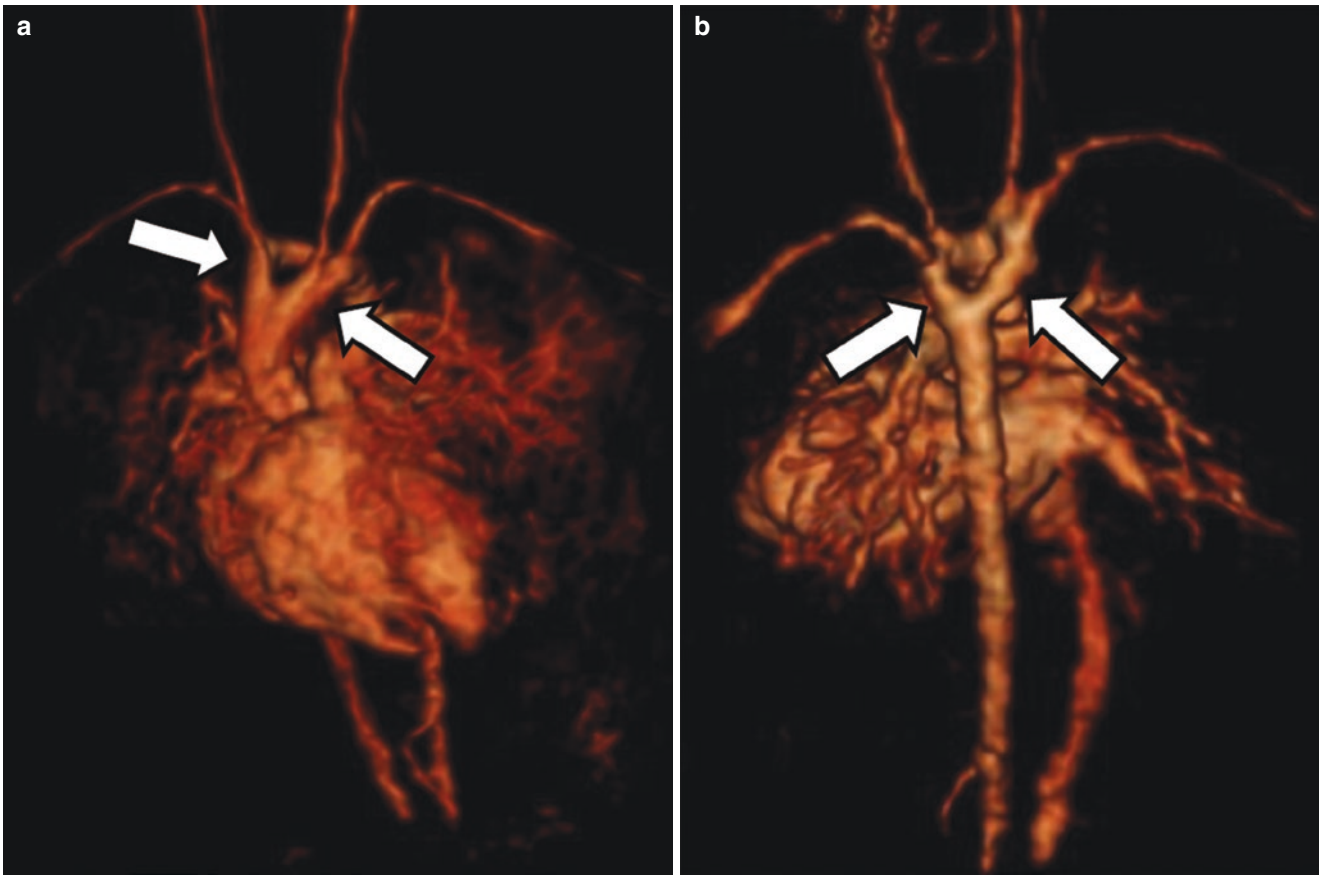

Fig. 21.2 A 1-year-old boy with double aortic arch. (**a**) Anterior oblique 3D volume-rendered image from contrast-enhanced time-resolved imaging of contrast kinetics (TRICKS) MR angiogram shows a double aortic arch (arrows). (**b**) Posterior 3D volume-rendered image from contrast-enhanced time-resolved imaging of contrast kinetics (TRICKS) MR angiogram shows a double aortic arch (arrows)

In this condition, the aortic arch is on the right, the left subclavian artery passes posterior to the esophagus, and the vascular ring is completed by a left-sided ductus arteriosus [15]. Most commonly, the left subclavian artery arises from a retroesophageal diverticulum of Kommerell [15]. The vascular ring in this condition is "looser" than the ring in a double aortic arch, and symptoms are typically less severe [22]. Treatment is with surgical division of the ligamentum arteriosus, and the diverticulum of Kommerell may also be resected [22].

Right-sided aortic arch may first be detected on chest radiography, demonstrating the aortic shadow to the right of the trachea, with leftward deviation of the trachea. Echocardiography typically also demonstrates the right-sided aortic arch. Cross-sectional imaging with CTA or MRA is indicated to evaluate the branching pattern. As previously discussed, MRA may be attempted with a "feed and swaddle" technique, but when not successful, the risks of ionizing radiation with CT must be weighed against the risks of sedation and anesthesia with MRI. On MRA of right aortic arch with an aberrant left subclavian artery, a single aortic arch is seen on the right, and the left subclavian artery typically arises from a dilated retroesophageal diverticulum of Kommerell [15, 24] (Fig. 21.3). The left ligamentum arteriosus may not be visible on MRI, although its presence may be inferred [27].

Pulmonary Artery Sling

Pulmonary artery sling is a rare vascular anomaly characterized by anomalous origin of the left pulmonary artery from the right pulmonary artery. The left pulmonary artery is located between the trachea and esophagus as it passes to the left hilum and typically causes compression of the right main bronchus and trachea. Extrinsic airway compression may lead to tracheobronchomalacia and air trapping [22, 27, 28]. In addition, intrinsic airway anomalies are associated with pulmonary artery sling including tracheobronchial branching anomalies and complete tracheal rings causing tracheobronchial stenosis [27, 28]. Pediatric patients with pulmonary artery sling typically present with respiratory symptoms within the first year of life, including stridor, wheezing, and recurrent pneumonia [22, 27, 28]. Surgical repair is recommended soon after diagnosis is established [22].

Diagnosis of pulmonary artery sling is typically made on MRI or CT, which are both well-suited to define the vascular anatomy and associated airway anomalies [27, 28]. The pri-

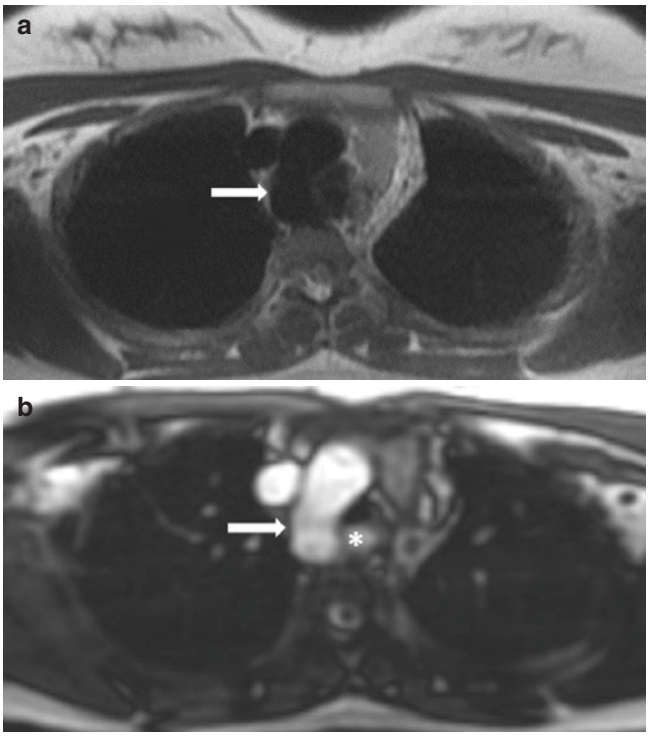

Fig. 21.3 A 12-year-old girl with right-sided aortic arch and aberrant left subclavian artery. (**a**) Axial 2D BB SSFSE MR image shows the abnormal position of arch the aortic (arrow), located on the right side of the mediastinum, consistent with the right aortic arch. (**b**) Axial 2D SSFP MR image demonstrates the right aortic arch (arrow) with an aberrant left subclavian artery (asterisk) passing posterior to the trachea and esophagus

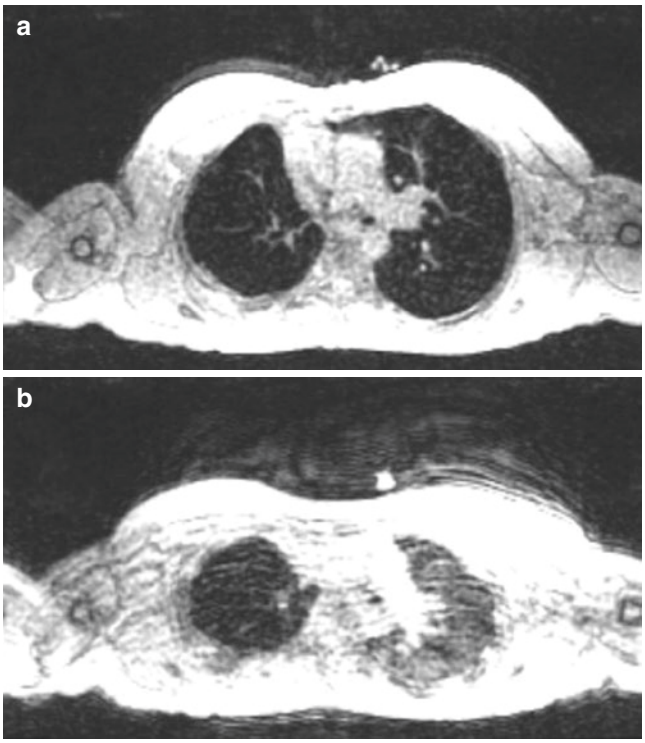

Fig. 21.4 A 11-year-old girl with pulmonary hypoplasia. (**a**) Axial 3D SPGR MR image obtained at end-inspiration demonstrates a smaller right lung compared to the left. (**b**) Axial 3D SPGR MR image obtained at end-inspiration shows a diffuse hypointensity of the right hypoplastic lung due to air trapping

mary advantage of MRI is its lack of ionizing radiation. However this benefit must be weighed against the risks of anesthesia, which is often required for MRI. Imaging is essential for surgical planning, and key elements to be assessed on MRI include pulmonary artery location and course, pulmonary artery caliber, airway branching pattern, airway caliber, and lung size to evaluate for air trapping [27]. 3D MRA sequences are ideal for characterization of the vascular anatomy. Nonfat-suppressed T1-weighted images are also excellent for depicting airway anatomy and assessing associated airway anomalies [27].

Congenital Lung Malformations

Pulmonary Hypoplasia

Pulmonary hypoplasia is a congenital anomaly of the pulmonary vasculature, airways, and parenchyma. Pulmonary hypoplasia is the least severe subtype of a larger group of pulmonary underdevelopment disorders which also include pulmonary agenesis and pulmonary aplasia [29]. Pulmonary agenesis is characterized by absent lung, airways, and vessels. Pulmonary aplasia has absent lung parenchyma and vessels, but a rudimentary bronchus is present. In pulmonary hypoplasia, the lung parenchyma, vessels, and airways are all present, but they are fewer and smaller than normal. The secondary form of pulmonary hypoplasia, in which a space-occupying process impedes pulmonary development, is most common. Primary pulmonary hypoplasia is encountered less frequently and can occur in isolation or in association with other conditions such as scimitar syndrome or horseshoe lung [30–33].

In the more common secondary form, pulmonary hypoplasia is often first appreciated on imaging studies in the context of the underlying space-occupying process. For example, in pulmonary hypoplasia secondary to congenital diaphragmatic hernia, the diagnosis is most often first appreciated on prenatal ultrasound or neonatal chest radiograph when intra-abdominal viscera are seen within the thorax. In these cases, postnatal MRI has less of a role in the diagnosis of pulmonary hypoplasia, but MRI may occasionally be performed to evaluate the hernia and visualize the size of the hypoplastic lung. In the less common primary form, thoracic MRI can play a large role in the diagnosis and management of pulmonary hypoplasia. In this scenario, a small lung may first be detected on chest radiograph, prompting work-up with cross-sectional imaging. MRI may then be obtained and show a small lung with small airways on standard T1- and T2-weighted images, and MRA may show small pulmonary arteries and veins (Fig. 21.4). MRI is also useful to evaluate

for associated conditions including scimitar syndrome, horseshoe lung, and congenital heart disease [34, 35].

Pulmonary Sequestration

Pulmonary sequestration is a congenital lung lesion characterized by an abnormal arterial supply from the systemic circulation and an abnormal tracheobronchial connection [36]. Pulmonary sequestration may be intralobar, in which the lesion shares a pleural covering with the adjacent normal lung and typically has venous drainage to the left atrium, or extralobar, in which the lesion has its own pleural covering and typically has venous drainage to a systemic vein [37–39]. Intralobar sequestration typically occurs in the lower lobes, and extralobar sequestration may occur in the lower lobes, below the diaphragm or within the mediastinum [37–39]. Pulmonary sequestration is at increased risk for pneumonia, and historically diagnosis was often established during the work-up of recurrent pneumonia. In current medical practice, most cases of pulmonary sequestration are first detected on prenatal sonogram as an incidental finding, in which a focal lung lesion is detected on gray-scale images and color Doppler demonstrates a systemic feeding artery [40]. Treatment for symptomatic pulmonary sequestration is surgical resection. Treatment for incidentally detected asymptomatic pulmonary sequestration is more variable and may involve watchful waiting or elective surgical resection due to concern about subsequent infection and small risk for malignancy [41, 42].

Cross-sectional imaging is indicated prior to resection in order to aid in surgical planning. In current practice, the preferred modality for this indication is most often CTA with 2D and 3D reformations rather than MRA given the superior temporal and spatial resolution without the need for sedation or anesthesia. The issue of spatial resolution is particularly important in pulmonary sequestration, as anomalous vessels are often small and better depicted on CTA than MRA. However, in cases where ionizing radiation is of significant concern, MRA is a potential alternative to CTA. On MRI, pulmonary sequestration typically appears as a cystic or solid mass-like lesion within the lung, which is hyperintense on fluid-sensitive sequences [43] (Fig. 21.5). MRA typically demonstrates a systemic feeding artery from the aorta and venous drainage to the left atrium (in intralobar sequestration) or a systemic vein (in extralobar sequestration) [43].

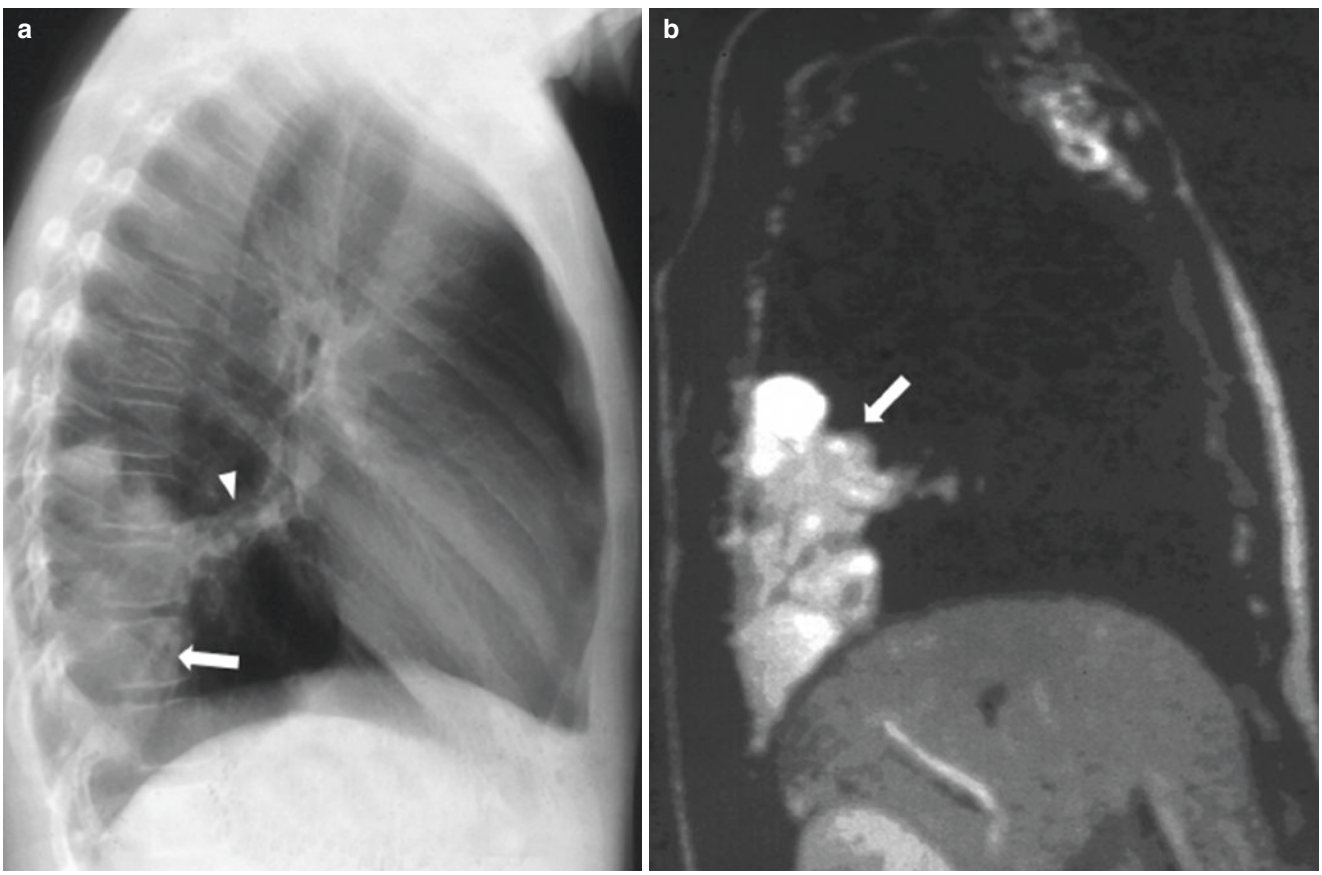

Fig. 21.5 Teenage boy with pulmonary sequestration. (**a**) Chest radiograph on left lateral view shows a large opacity (arrow) involving the dorsal region of the right lower lobe with a vascular connection (arrowhead) to the right hilum. (**b**) Sagittal T2-weighted fat-suppressed MR image shows a heterogeneous hyperintense mass-like lesion (arrow) confirmed after surgical resection as pulmonary sequestration. (Courtesy of Dr G Morana, Treviso, Italy)

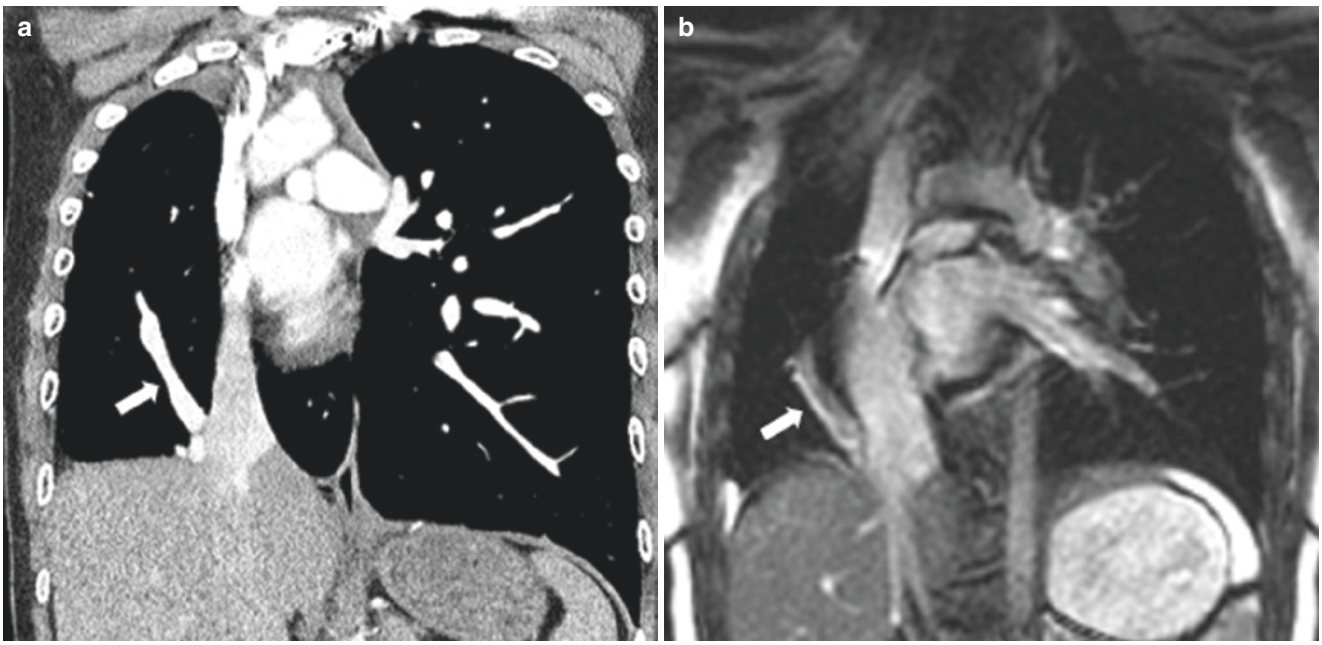

Fig. 21.6 A 11-year-old girl with scimitar syndrome. (**a**) Coronal contrast-enhanced CT image demonstrates a hypoplastic right lung drained by an anomalous vein (arrow) which is connected to the inferior vena cava. (**b**) Coronal 2D FIESTA MR image shows a hypoplastic right lung drained by an anomalous vein (arrow) which is connected to the inferior vena cava

Scimitar Syndrome

Scimitar syndrome, also known as congenital venolobar syndrome, is a congenital condition characterized by right lung hypoplasia and partial anomalous pulmonary venous return in which the anomalous vein drains the right lung into the inferior vena cava [44]. The name scimitar syndrome is derived from the appearance of the anomalous vein on chest radiography, which resembles a Turkish sword. Patients with scimitar syndrome may present to medical attention due to symptoms related to left-to-right shunting, associated congenital heart disease, or the findings may be incidentally noted on chest radiographs or other imaging tests. Patients presenting in infancy have more symptoms, aortopulmonary collaterals, coexisting congenital heart disease, extracardiac anomalies, and pulmonary hypertension than patients presenting later in life [45]. The optimal management strategy is controversial. Asymptomatic patients without significant shunting may be managed medically to prevent or control pulmonary hypertension [44]. Symptomatic patients with significant shunting may be treated surgically by reimplanting the scimitar vein into the left atrium or creating an intracardiac baffle between the scimitar vein ostium and the left atrium [44]. Mortality and vein stenosis/obstruction after baffle repair or scimitar vein reimplantation are higher for patients with infant-onset disease than for patients who present later [46].

When scimitar syndrome is suspected, cross-sectional imaging with CT or MRI with 2D and 3D angiographic reconstructions is recommended for confirmation of the diagnosis, mapping the anomalous vein, and surgical planning. MRI provides an advantage over CT, as it is able to quantify the Qp/Qs shunt ratio with phase-contrast sequences, and Qp/Qs >1.5 is an indication for surgery [44]. Both MRA and CTA are well-suited to depict the anatomy of the scimitar vein or veins, which may show a scimitar vein or veins draining one, two, or three lobes of the lung into the supradiaphragmatic or infradiaphragmatic IVC [44] (Fig. 21.6). Additional findings associated with scimitar syndrome that may be detected on MRI include pulmonary sequestration, accessory diaphragm, diaphragmatic hernia, variant lobar anatomy, right lung hypoplasia, right pulmonary artery hypoplasia, enlarged pulmonary arteries, congenital heart disease, aortic arch anomalies, right ventricular enlargement, dextroposition of the heart, and vertebral anomalies [44].

Nonvascular Thoracic Anomalies and Abnormalities

With increased utilization of cardiac MRI, most appreciate the potential role for MRI of the chest to evaluate the heart and mediastinal vasculature. MRI of the thorax for nonvascular lesions has been less widely adopted, largely because of the widespread availability and excellent imaging quality of CT for these indications. CT often provides the additional advantage of not requiring sedation or general anesthesia, which are often required for MRI in young uncooperative children. MRI provides the distinct advantage of not utilizing

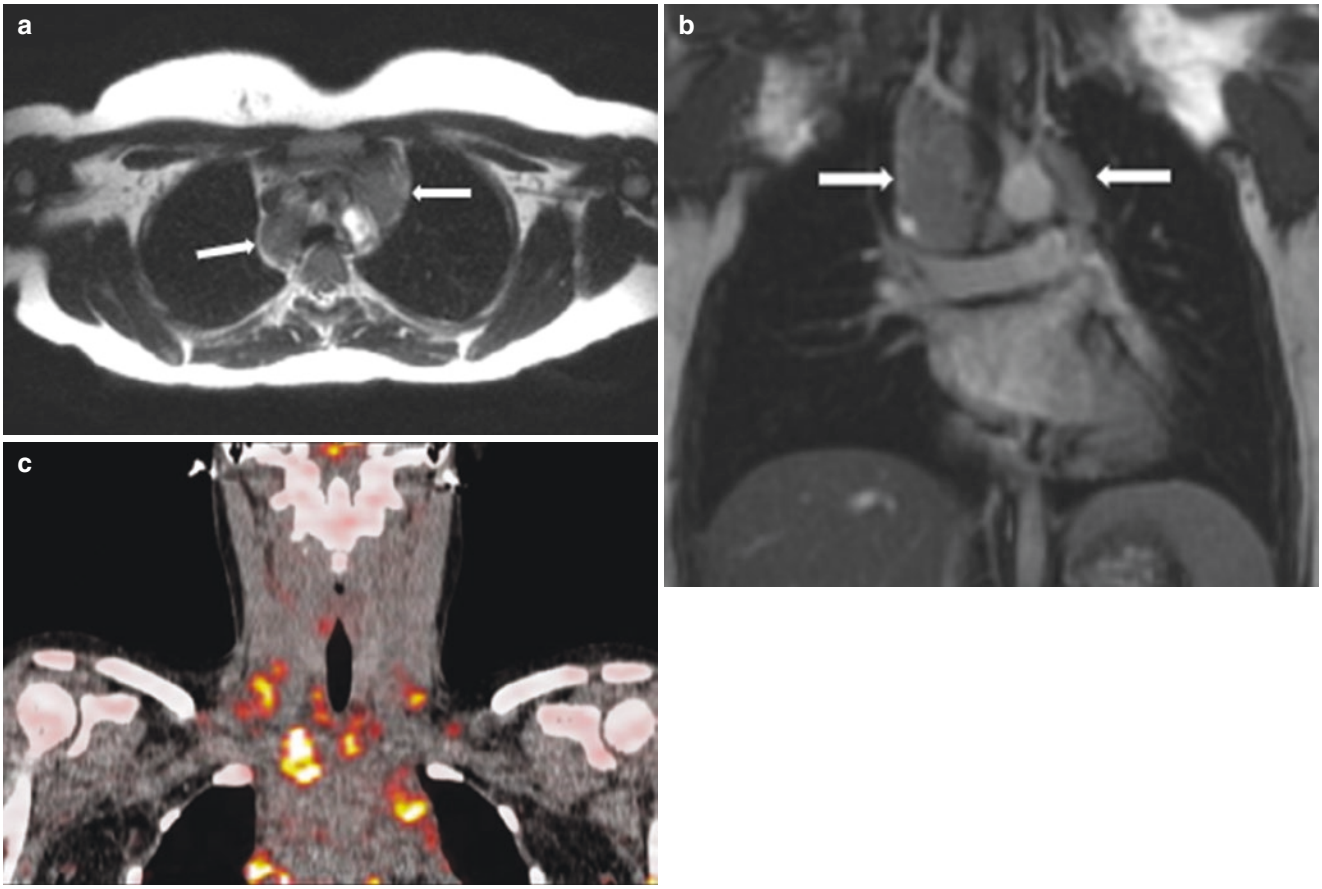

Fig. 21.7 A 12-year-old girl with Hodgkin lymphoma. (**a**) Axial T2-weighted HASTE MR image shows mediastinal lymphadenopathy (arrows). (**b**) Coronal contrast-enhanced T1-weighted FIESTA MR image shows mediastinal lymphadenopathy (arrows). (**c**) Fluoro-deoxyglucose (FDG) PET/CT MR image shows intense FDG uptake by the mediastinal lymph nodes

ionizing radiation, and as the imaging quality of MRI has improved in recent years, there has been increased interest in performing more imaging studies of the chest with MRI rather than CT. This might be most pertinent to children who can cooperate for MRI without sedation and would therefore potentially reap the benefit of a diagnostic study without risks of exposure to ionizing radiation or sedating medications. Potential nonvascular applications for MRI of the thorax described here include mediastinal masses, infectious disorders, lung anomalies, and airway disorders.

Mediastinal Masses

Lymphoma

Lymphoma is the third most common malignancy among patients aged 0–19 years [47]. It is the most common cause of an anterior mediastinal mass in a child [48, 49]. The currently recommended modality for staging of lymphoma is FDG-PET/CT [50]. However, FDG-PET/CT requires the use of ionizing radiation, which is of particular concern in children who require multiple staging examinations through the course of treatment. Due to these concerns, there is increased interest in whole-body MRI as a potential alternative for staging lymphoma [50]. Recommended protocols include T1-weighted, T2-weigthed STIR, and diffusion-weighted sequences [50]. Initial studies suggest good agreement between FDG-PET/CT and whole-body MRI for the staging of lymphoma [50].

Anesthesia is often required for MRI in young children who are unable to cooperate with instructions, but this can be a risk in lymphoma. Large anterior mediastinal masses may cause airway compression, obstruction of venous return, or obstruction of cardiac output, which may be exacerbated by general anesthesia [51]. When imaging an anterior mediastinal mass, it is essential to do so carefully and with as little sedation as possible. Furthermore, surgical procedures must also be approached with caution, and assessment of airway and vascular compression on cross-sectional imaging is essential to surgical and anesthesia planning [48, 49, 51].

The most common intrathoracic findings of lymphoma on MRI include an anterior mediastinal mass and lymphadenopathy (Fig. 21.7). When an anterior mediastinal mass is present due to thymic involvement, MRI typically shows an enlarged heterogeneous thymus on T1- and T2-weighted

images and increased signal intensity on diffusion-weighted images [50]. On T1- and T2-weighted images, lymph nodes can be assessed in a similar fashion as on CT and are considered enlarged when measuring greater than 1 cm in short-axis diameter. As discussed previously, assessment of airway compression is essential and is well evaluated on nonfat-suppressed T1-weighted MR images [52].

Teratoma

Germ cell tumors are the second most common anterior mediastinal mass in children after lymphoma [53]. Germ cell tumors are thought to derive from pluripotential primitive germ cells. Germ cell tumors most commonly occur in the gonads, but can occur outside the gonads along the midline of the body, 4% of which arise in the mediastinum [54]. The majority of mediastinal germ cell tumors are benign mature teratomas [53, 55]. Malignant mediastinal germ cell tumors include seminoma, embryonal carcinoma, teratocarcinoma, choriocarcinoma, and endodermal sinus tumor. Mediastinal teratomas may present with symptoms of respiratory distress, cough, chest pain, and weight loss, but approximately half of benign mature teratomas are incidentally detected on imaging performed for another reason [56]. The treatment for benign mature cystic teratoma is surgical resection, which is curative [53, 55, 56]. Treatment of malignant germ cell tumors depends on the type and extent of disease, but may include resection, chemotherapy, radiation therapy, or a combination [53, 55, 56].

Mature teratomas contain tissues from all three embryological layers, and the imaging appearance reflects the presence of multiple tissue types. Masses are most often located in the anterior mediastinum, demonstrate well-demarcated borders, and may contain cystic elements, fat, and calcification [57]. Although CT is most often utilized in the evaluation of mature teratomas, MRI is also well suited to characterize the different tissue compositions of the mass, given its superior contrast resolution. MRI findings may include a heterogeneous mass with cystic elements that are hyperintense on T2-weighted images and hypointense on T1-weighted images [57] (Fig. 21.8). Fat is often present and appears hyperintense on T1-weighted nonfat-suppressed images [57]. In and out of phase imaging demonstrates chemical shift artifact at fat-soft tissue interfaces, and fat-suppressed sequences may confirm presence of fat by showing signal loss compared to nonfat-suppressed sequences [58]. Malignant mediastinal germ cell tumors typically appear as solid enhancing mediastinal masses, which may invade adjacent structures. Superior contrast resolution makes MRI ideal for demonstrating violation of adjacent fat planes and extension to adjacent structures [57].

Lipoma

Lipomas are benign fat-containing masses, which are rare in children. Thoracic lipomas may occur in the mediastinum or chest wall. Mediastinal lipomas most often occur in the anterior mediastinum. They are most often asymptomatic and incidentally noted on chest radiography [58]. Symptoms may rarely occur due to mass effect and may include dysphagia, dyspnea, cough, jugular distention, and cardiac arrhythmias [58]. Surgical excision is curative and only necessary in patients with symptoms. The appearance on MR is a homogenous well-demarcated mass which is hyperintense on T1-weighted nonfat-suppressed sequences with signal loss on fat-suppressed sequences (Fig. 21.9).

Mediastinal lipomas should not be confused with lipoblastomas, which are also benign fat containing masses but have a different imaging appearance. Lipoblastomas are masses seen in young children, most detected before 3 years of age [59]. Unlike lipomas which are uniformly composed of fat, lipoblastomas contain prominent stromal elements. The MR imaging appearance of lipoblastoma is a mass which contains fat that is hyperintense on T1-weighted nonfat-suppressed sequences and loses signal on fat-suppressed sequences along with linear areas of soft tissue and fluid signal representing the fibrovascular network and cystic changes [58].

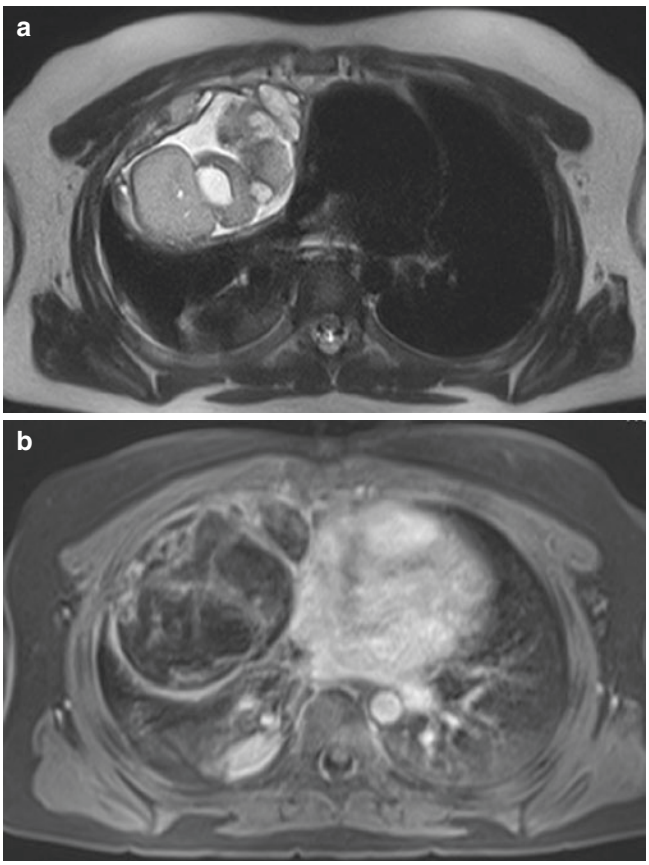

Fig. 21.8 A 14-year-old girl with mediastinal teratoma. (**a**) Axial T2-weighted HASTE MR image demonstrates a mediastinal mass with inhomogeneous signal intensity due to cystic and solid components. (**b**) Axial contrast-enhanced T1-weighted THRIVE MR image with fat suppression shows hyperenhancement of the wall and soft tissue components of the mass

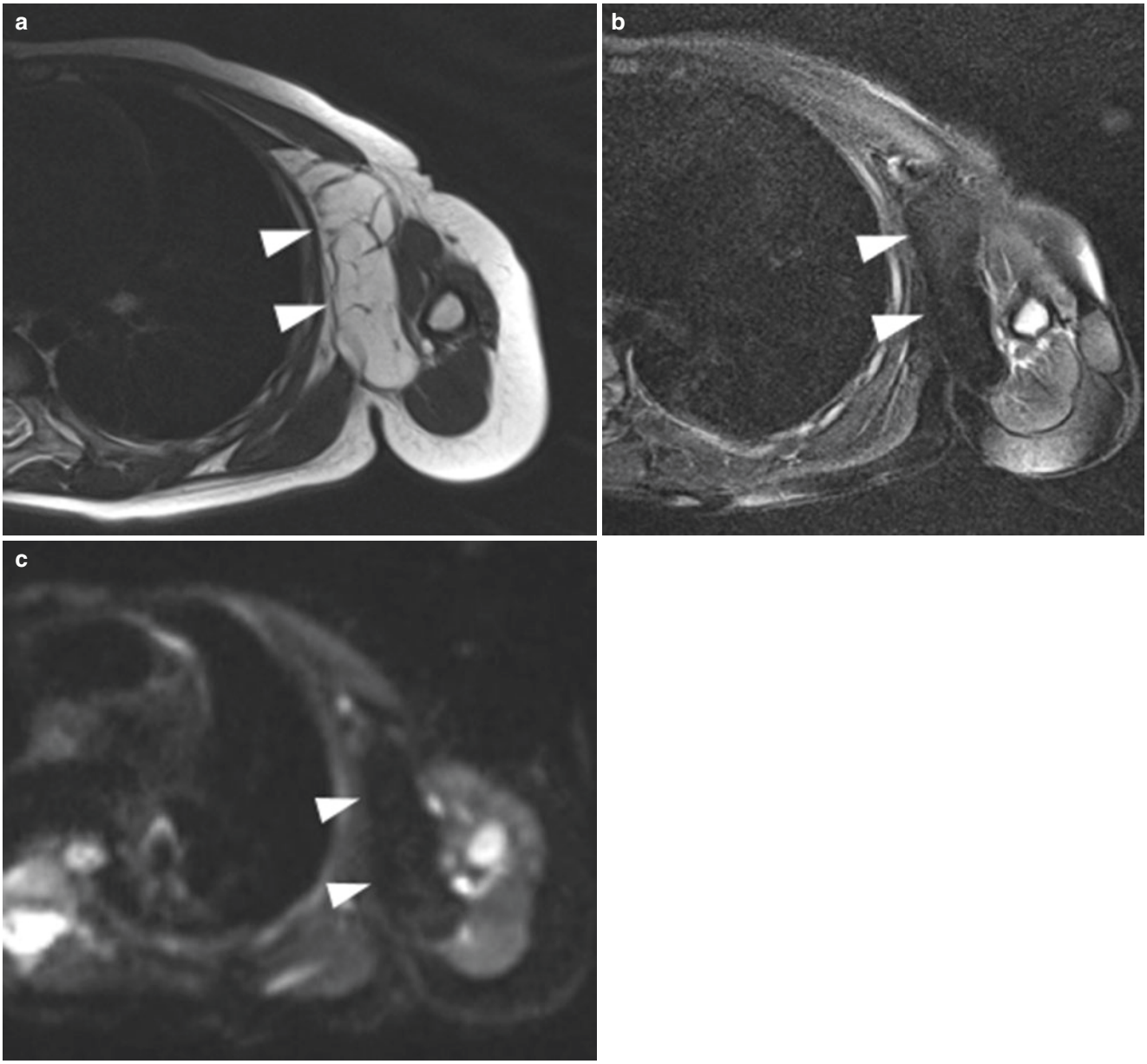

Fig. 21.9 A teenage boy with chest wall lipoma. (**a**) Axial T1-weighted BLADE MR image demonstrates a hyperintense multiseptated well-circumscribed mass (arrowheads) located in the left chest-wall. (**b**) Axial T2-weighted BLADE MR image with fat suppression shows a loss of signal within the mass (arrowheads), indicating fat. (**c**) Axial DWI MR image does not show restricted diffusion within the mass (arrowheads), indicating low cellularity

Neuroblastoma

Approximately 90% of posterior mediastinal masses in children are neurogenic tumors arising from the paraspinal sympathetic chains [60, 61]. Most of these are neuroblastomas, which are malignant tumors derived from neural crest cells. The majority of neuroblastomas occur in the adrenal glands; however, up to 20% occur within the posterior mediastinum [60]. Signs and symptoms may include fever, irritability, weight loss, anemia, and Horner syndrome if in the superior mediastinum [60]. Differential considerations for a posterior mediastinal mass include related neurogenic tumors that also arise from the sympathetic chain, including ganglioneuroblastoma and ganglioneuroma. Nerve sheath tumors are another differential consideration and include neurofibroma and schwannoma. The preferred treatment for neuroblastoma is surgical resection and chemotherapy [60].

MRI is the preferred imaging modality for the diagnosis and staging of mediastinal neuroblastoma due to its lack of ionizing radiation and superior ability to depict neuroforaminal and extradural intraspinal extension [61]. MRI is also well suited to detection of metastatic disease, which most commonly involves the liver, bone, bone marrow, and local

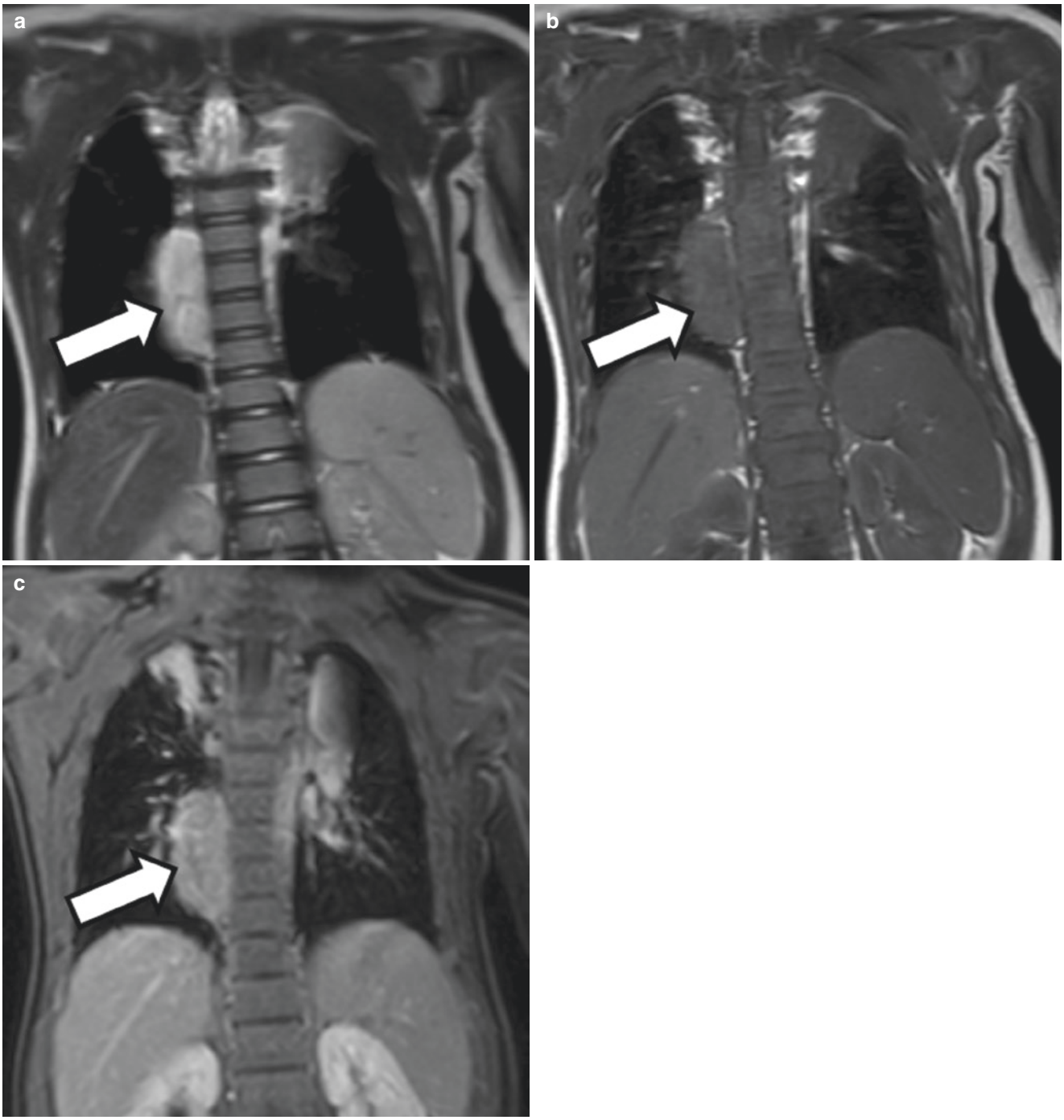

Fig. 21.10 A 19-month-old girl with thoracic neuroblastoma. (**a**) Coronal T2-weighted MR image shows a right paraspinal mass (arrow), which is hyperintense to the adjacent skeletal muscle. (**b**) Coronal T1-weighted MR image shows a right paraspinal mass (arrow), which is mildly hyperintense to the adjacent skeletal muscle. (**c**) Coronal enhanced T1-weighted MR image with fat suppression shows a right paraspinal mass (arrow), which is hyperenhancing compared to the adjacent skeletal muscle

lymph nodes. MRI does not depict calcification as well as CT, which is present in up to 30% of cases [60]. The typical appearance of neuroblastoma is an infiltrating mass which surrounds and encases vessels and adjacent structures. On MRI, neuroblastoma is typically heterogeneously hyperintense to skeletal muscle on T2-weighted images, mildly hyperintense on T1-weighted images, and heterogeneously enhances on contrast-enhanced images (Fig. 21.10).

Infectious Disorders

Tuberculosis

Although tuberculosis (TB) has become rare in the developed world, it continues to be a major cause of morbidity and mortality in the developing world. Worldwide, 12 million people are estimated to have active TB, and 1.5 million deaths are attributed to TB every year [62]. In the developed

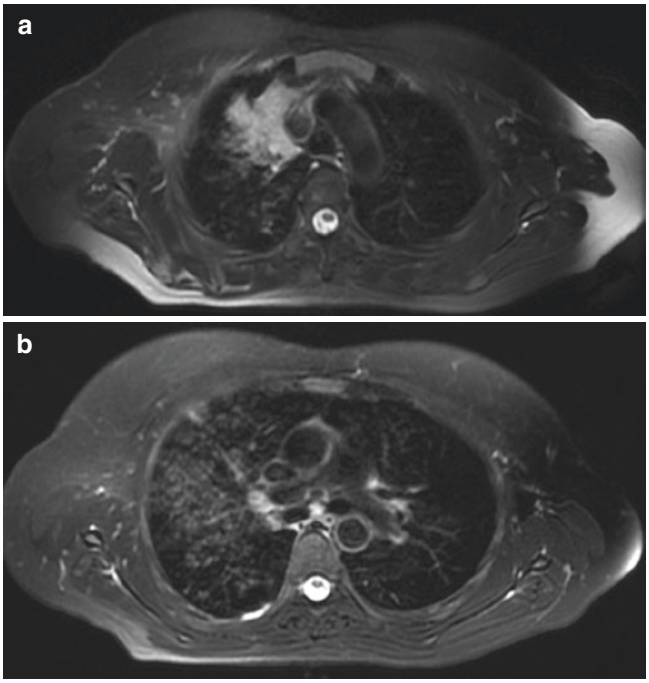

Fig. 21.11 A 16-year-old girl with tuberculosis. (**a**) Axial T2-weighted FRFSE MR image with fat suppression shows parenchymal consolidation in the right upper lobe. (**b**) Axial T2-weighted FRFSE MR image with fat suppression acquired at a lower level demonstrates mucus plugging with "tree in bud" appearance in the right lung

world, TB most often affects those with lower income, migrants, and immunodeficiency [63]. The initial infection is referred to as primary TB and occurs when an exposed individual inhales respiratory droplets, and infection occurs within the lung. Primary infection most often causes mild symptoms of fever and cough. Symptoms can be more severe in progressive primary TB and may lead to significant airspace disease and intrathoracic adenopathy which may compress the airway [64, 65]. After primary infection the symptoms often improve, and infection becomes dormant. Reactivation TB can occur when infection worsens, and symptoms may include fever, weight loss, night sweats, productive cough, chest pain, and hemoptysis.

Imaging plays an important role in the management of TB, and chest radiography and CT are the main modalities used. MRI is less often utilized given the higher cost, more limited availability, and technical challenges, but can be considered in children who may require multiple imaging studies in order to reduce exposure to ionizing radiation, such as those with immunodeficiency. MRI findings in pulmonary TB may include consolidation with or without cavitation, ground-glass signal abnormality, pulmonary nodules, lymphadenopathy, and pleural effusion [66, 67] (Fig. 21.11). It has been suggested that MRI may be superior to CT for evaluation of nodal disease and pleural effusion in TB infection [66]. T2- and STIR-weighted sequences may show pulmonary necrosis in TB as a region of low signal intensity centered within a region of consolidation [67]. However, MRI is known to be less sensitive than CT for ground-glass and tree-in-bud signal abnormalities [66].

Histoplasmosis

Histoplasmosis is endemic to many regions and infection is common. Infection most often causes only mild symptoms [68]. However, immunocompromised children may experience severe infection [68]. Infection may lead to intrathoracic lymphadenopathy, pulmonary consolidation, pulmonary nodules, cavitation, and bronchiectasis. A potential complication of histoplasmosis infection is mediastinal fibrosis.

MRI is not utilized in the routine management of histoplasmosis, though it may be considered in patients with concern about ionizing radiation, such as immunocompromised children who may require multiple imaging studies over their lifetimes. There is very little published literature describing the findings of pulmonary histoplasmosis on MRI. MRI findings may include enlarged intrathoracic lymph nodes, ill-defined pulmonary nodules, and pulmonary consolidation, all of which are hyperintense on T2-weighted images [69] (Fig. 21.12).

Aspergillosis

Aspergillus fumigatus is an airborne fungus that is ubiquitous within the environment [70]. In normal immunocompetent children, inhalation of the fungus most often causes no symptoms or illness. *Aspergillus*-related lung disease may occur in children with immunodeficiency or underlying lung disease, and the manifestations depend on the immunologic status of the child [70]. Three different forms of pulmonary aspergillosis include aspergilloma within a preexisting cavity, allergic bronchopulmonary aspergillosis (ABPA), and invasive aspergillosis.

Pulmonary aspergillosis is most often diagnosed and managed on the basis of chest radiographs and CT. MRI might be considered for children in whom there is concern about the effects of ionizing radiation, although there are few descriptions of MRI findings in pulmonary aspergillosis in the medical literature. Pulmonary aspergilloma appears as a "fungus ball" within a cavity that is hypointense on both T1- and T2-weighted images [71]. ABPA appears as dilated bronchi and bronchioles containing impacted material which is hyperintense on T1-wieghted images and hypointense on T2-wieghted images [72, 73] (Fig. 21.13). The signal characteristics of the impacted material are the opposite of water, and this pattern is called the inverted mucoid impaction signal sign, which is characteristic for ABPA [72, 73]. Invasive aspergillosis appears as round and nodular areas of signal abnormality, which classically have the appearance of a "target." The "target" is formed by an outer portion demonstrating high signal intensity on T1- and T2-weighed images and enhancement on post-contrast images surrounding a central area of hypointensity [74, 75].

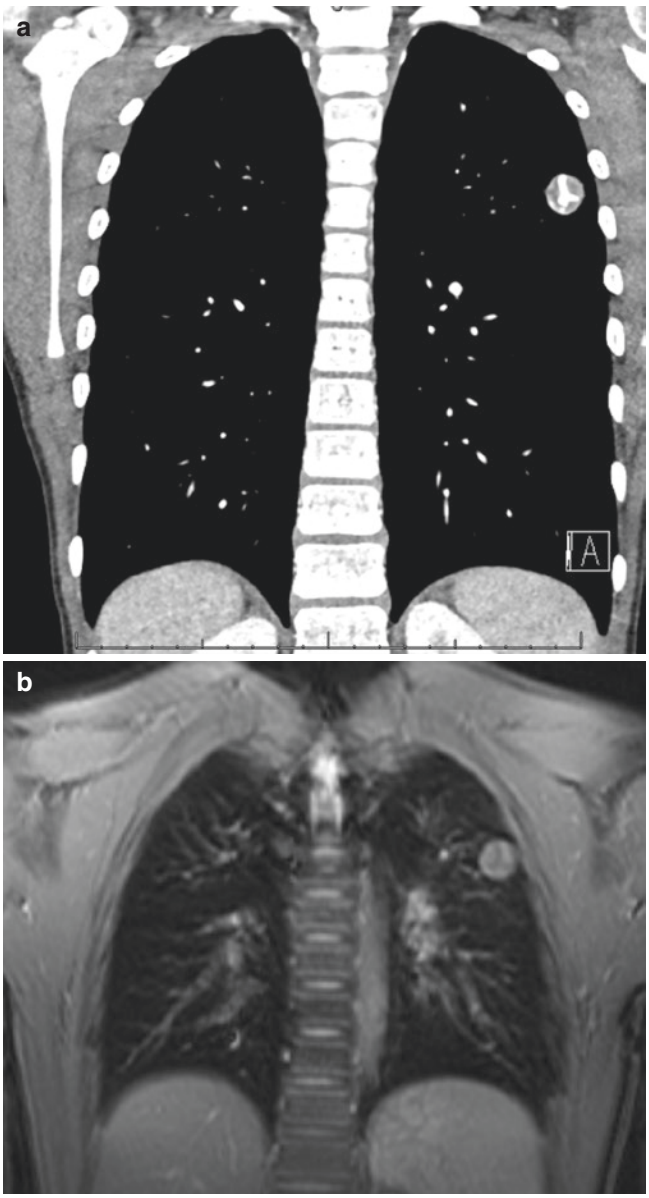

Fig. 21.12 A 9-year-old boy with histoplasmosis. (**a**) Coronal contrast-enhanced CT image in soft tissue window setting shows a round nodule within the left upper lobe with central calcification. (**b**) Coronal contrast-enhanced LAVA MR image shows the left upper lobe nodule with a hypointense non-enhancing central portion at the site of calcification

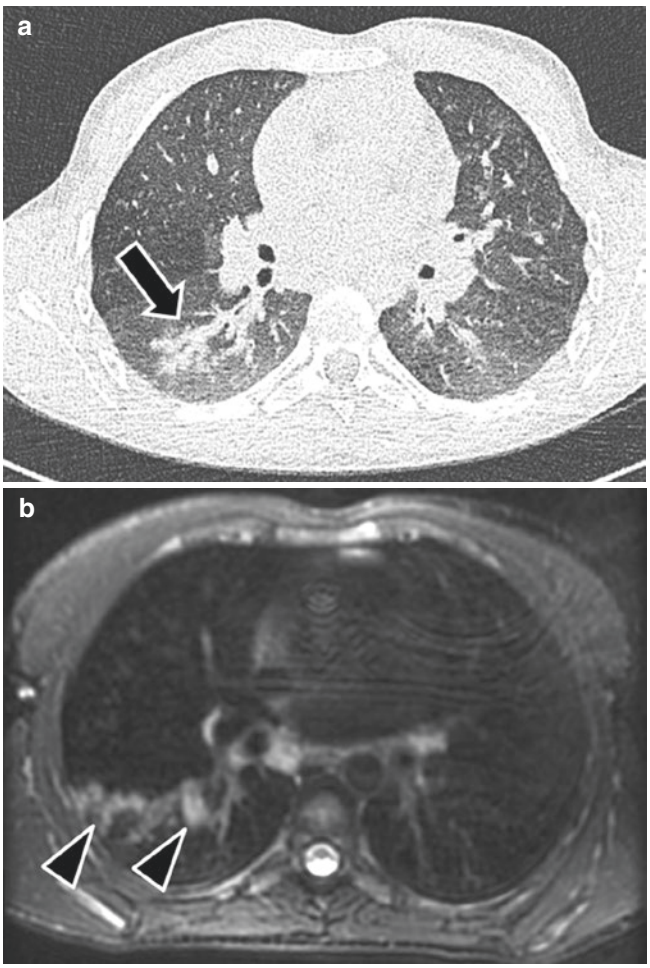

Fig. 21.13 A 12-year-old boy with cystic fibrosis and *Aspergillus* infection. (**a**) Axial non-enhanced lung window setting CT image shows right lower lobe bronchiectasis containing impacted material (arrow). (**b**) Axial T2-weighted MR image with fat suppression shows right lower lobe bronchiectasis containing impacted hyperintense mucus (black arrowheads) due to *Aspergillus*

Lung Anomalies and Abnormalities

Congenital Pulmonary Airway Malformation

Congenital pulmonary airway malformations (CPAMs) (previously known as congenital cystic adenomatoid malformations (CCAMs)) are malformations of the lung which are composed of cysts and bronchiolar overgrowth without a normal connection with the airway [37, 39]. Cysts may range in size from microscopic to large. Large cysts are visible on gross inspection and imaging. When composed of microscopic cysts, the appearance is that of a solid mass on gross inspection and on imaging. CPAMs are frequently diagnosed on prenatal ultrasound and are asymptomatic at birth. CPAMs are at risk for superinfection and may present with infectious symptoms at the time of superinfection. Surgical resection is the preferred treatment for symptomatic CPAMs. Asymptomatic CPAMs may be removed due to risk for subsequent superinfection and small risk of malignancy or may be managed conservatively with a watchful waiting approach [76–81].

Radiologists most commonly use the updated and modified Stocker classification system when describing CPAMs [37, 39, 82–86]. In this system, there are five types of CPAM.

Type 0 CPAMs are incompatible with life and cause diffuse acinar dysgenesis or tracheobronchial dysplasia. Type 1 CPAMs are macrocytic, containing one or more cysts measuring >2 cm. Type 2 lesions are composed of

smaller macrocysts measuring <2 cm. Type 3 CPAMs are microcystic and appear as solid masses on gross inspection and imaging, but small cysts <5 mm are evident at microcopy. Type 4 lesions are characterized by large cysts located within the periphery of the lung and appear similar to Type 1 CPAMs.

CPAMs may be visible on neonatal chest radiograph as an air-filled cystic lesion or a solid mass, depending on the type [87]. Alternatively, a CPAM detected on prenatal ultrasound may not be visible on chest radiographs after birth [38–40]. When surgical resection is being considered, cross-sectional imaging is required to localize and evaluate the lesion. Although classic CPAMs are not associated with anomalous vascular supply, cross-sectional imaging with 2D and 3D angiographic technique is advised since pulmonary sequestration and hybrid lesions (combined CPAM and sequestration) are often differential considerations. In current practice this is most often achieved with contrast-enhanced CTA. Contrast-enhanced MRI with MRA can be considered as an alternative to CTA in certain situations, such as when there is substantial concern for radiation exposure. Fluid-filled Type 1, 2, and 4 CPAMs are well-seen on T2-weighted images as hyperintense cysts, which on contrast-enhanced images demonstrate a thin enhancing wall [43]. Air-filled Type 1, 2, and 4 CPAMs are not as easily seen on MRI, since the air-filled cyst may appear similar to the adjacent aerated lung [43]. Type 3 CPAMs are well visualized on contrast-enhanced images as a solid enhancing mass (Fig. 21.14).

Lymphangiectasia

Pulmonary lymphangiectasia is a congenital condition characterized by dilated pulmonary lymphatics and chylous pleural effusions [88, 89]. It is associated with congenital heart disease, trisomy 21 and Noonan syndrome [90]. Newborns with pulmonary lymphangiectasia typically present with severe respiratory symptoms. In the past, pulmonary lymphangiectasia was considered to be a fatal condition, but mortality rates have decreased due to improvements in treatment and better survival among affected patients with a late-onset form of the condition [89–91]. Pulmonary lymphangiectasia is often challenging to diagnose, but may be suggested by performing thoracentesis after a fatty meal, and pleural fluid will be chylous.

Imaging findings are somewhat nonspecific in pulmonary lymphangiectasia, but imaging is essential to the evaluation and work-up of the condition. Radiographs and CT are the most commonly utilized modalities in this condition. Chest radiographs typically show interstitial thickening and pleural effusion, and CT typically shows interlobular septal thickening, ground-glass opacities, and pleural effusion [91, 92]. MRI is not routinely performed for this indication, but patients with congenital heart disease-related pulmonary lymphangiectasia may have an MRI during the work-up of cardiac disease, and findings may be detected. Findings on MRI are similar to the findings on CT and include interlobular septal thickening which is hyperintense on T2-weighted images and pleural effusion [43].

Cystic Fibrosis

Cystic fibrosis (CF) is an inherited autosomal recessive disease caused by mutations in the CF transmembrane regulator (CFTR) gene. CF is the most common autosomal recessive disease in Caucasians [93]. The mutation leads to decreased transmembranous chloride transport causing secretions to be thick and viscous, leading to manifestations with the lung, gastrointestinal tract, and exocrine systems. In the neonatal period, affected patients may be asymptomatic, have respiratory symptoms, or present with meconium ileus. Screening blood tests for CF are now included with newborn screening in all 50 states in the USA, and diagnosis is often established before substantial symptoms occur.

Pulmonary manifestations of CF include air trapping, mucus impaction, airway wall thickening, and bronchiectasis [94–96]. Imaging plays a key role in monitoring disease progression and offers many advantages over pulmonary function tests (PFTs) alone [96]. CT has served as the reference standard for CF, and established advantages of CT over PFTs include evaluation of regional disease severity, greater sensitivity for detection of disease progression, and detection of structural changes before PFTs become abnormal [96]. However, CF is a lifelong disease, and numerous imaging tests are required over a patient's lifetime. Repeated CTs have the potential to lead to large cumulative radiation doses. As a result, MRI has emerged as an alternative imaging modality that does not require ionizing radiation [97]. Although the spatial resolution of MRI is lower than CT, increased signal associated with bronchiectasis, mucus plugging, and consolidation on MRI leads to improved contrast resolution, and sensitivity of MRI for these findings is comparable to CT [96, 98–100] (Fig. 21.15). Advanced MRI techniques including contrast-enhanced perfusion imaging and hyperpolarized gas ventilation imaging can provide functional information not available on CT [96]. New ultrashort echo time (UTE) sequences which overcome issues of rapid signal dephasing and low spatial resolution to produce "CT-like" images of the lung will likely further enhance the role of MRI in the evaluation of CF-related lung disease in the future [96, 101].

Common Variable Immunodeficiency

Common variable immunodeficiency (CVID) is a primary immunodeficiency syndrome characterized by low immunoglobulin levels. The syndrome may be caused by a variety of different genetic mutations. Clinical manifestations in a cohort of 473 patients described by Resnick et al. include recurrent

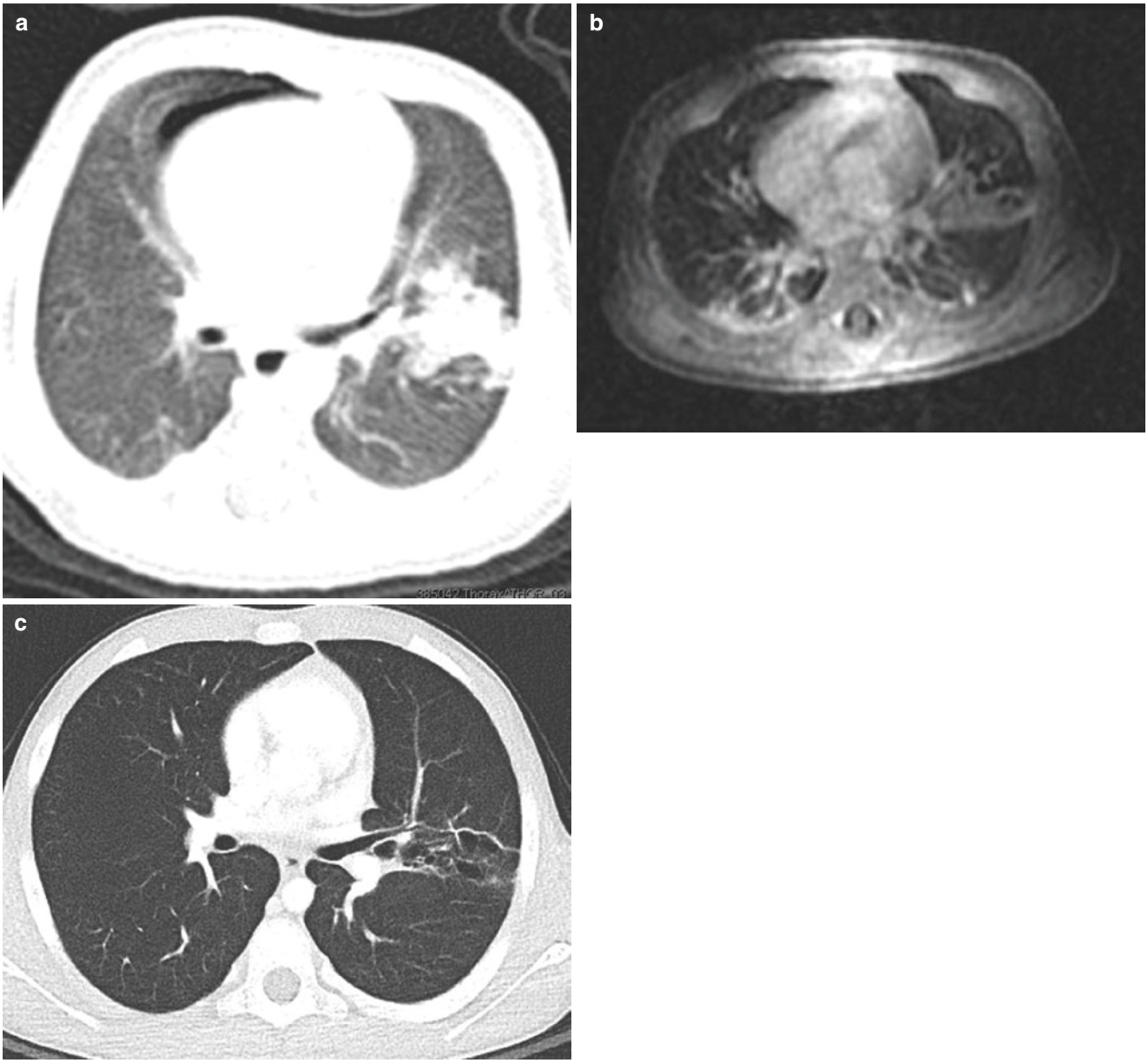

Fig. 21.14 A 3-year-old girl with congenital pulmonary airway malformation (CPAM) imaged at three different time points. (**a**) Axial non-enhanced lung window CT image obtained at day 1 of life shows consolidation within the left lower lobe. Small right pneumothorax is incidentally noted. (**b**) Axial contrast-enhanced SPGR MR image obtained at 6 months of age shows persistent consolidation within the left lower lobe. (**c**) Axial contrast-enhanced lung window setting CT image obtained at 8 years of age shows cystic appearance of left lower lobe CPAM after clearance of consolidation

infections (94%) and noninfectious complications including hematologic or organ-specific autoimmunity (28.6%), chronic lung disease (28.5%), bronchiectasis (11.2%), gastrointestinal inflammatory disease (15.4%), malabsorption (5.9%), granulomatous disease (9.7%), liver diseases and hepatitis (9.1%), lymphoma (8.2%), and other cancers (7.0%) [102]. Most cases of CVID are diagnosed in adulthood, but as many as 34% are diagnosed during childhood [103].

Pulmonary manifestations of CVID include pneumonia, chronic lung disease, and bronchiectasis. Imaging plays a key role in the diagnosis and management of these complications. Although CT is an excellent modality for the evaluation of these findings, patients with CVID are more susceptible to radiation-induced malignancy making MRI an attractive alternative [104, 105]. MRI findings in CVID may include consolidation, bullae, nodules, air trapping, and bronchiectasis with bronchial wall thickening and mucus plugging (Fig. 21.16).

In studies of patients with CVID, lung MRI was similar to CT for detection of moderate-to-severe disease including consolidation, bullae, mucus plugging, nodules, bronchial

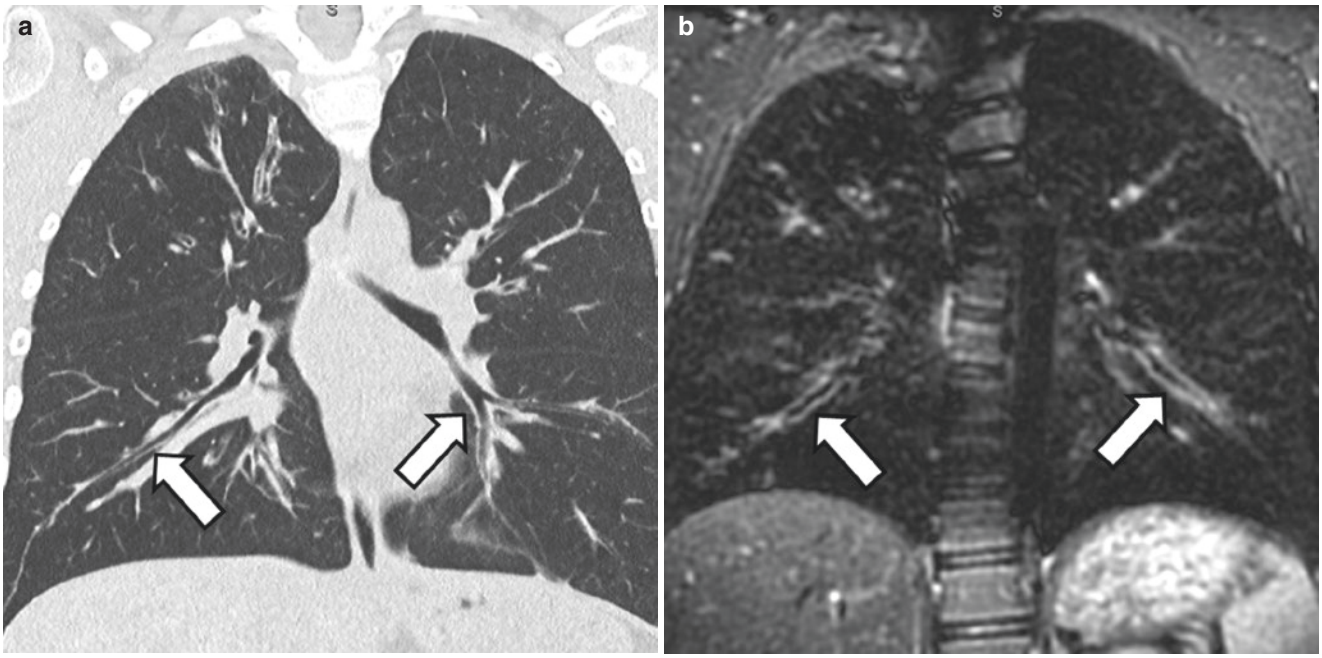

Fig. 21.15 A 13-year-old boy with cystic fibrosis. (**a**) Coronal non-enhanced lung window setting CT image shows bronchiectasis and bronchial wall thickening (arrows) in both lower lobes. (**b**) Coronal T2-weighted MR image with fat suppression shows bronchiectasis and hyperintense bronchial wall thickening (arrows) in both lower lobes

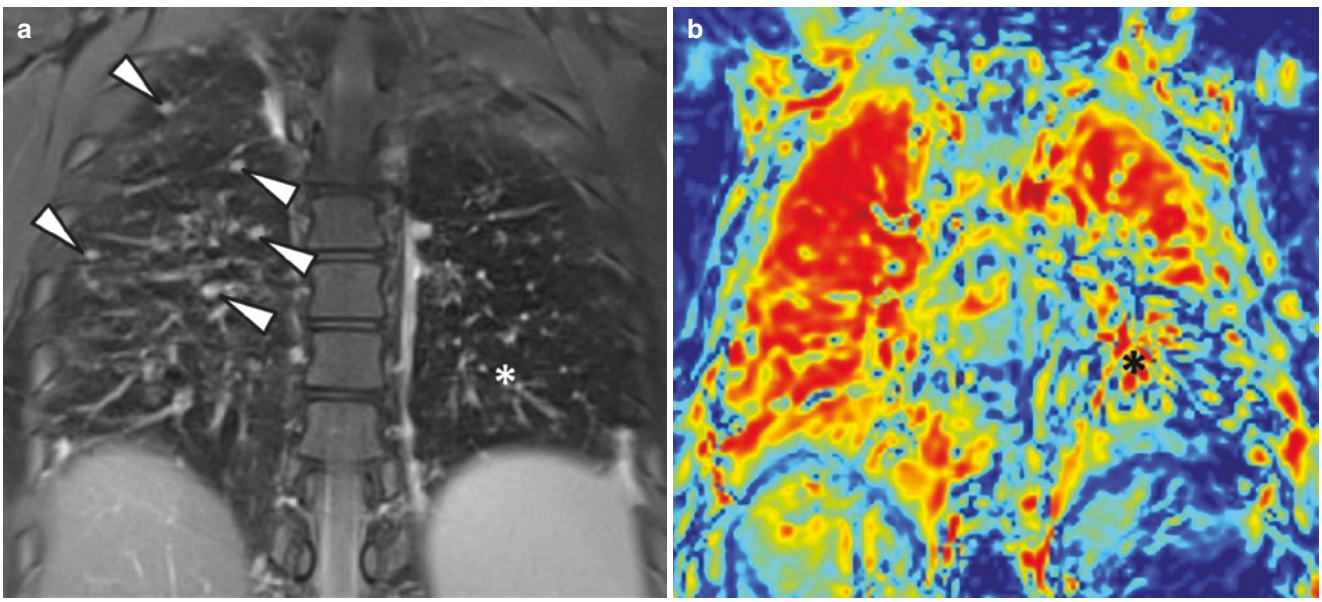

Fig. 21.16 A 19-year-old-girl with common variable immunodeficiency. (**a**) Coronal T2-weighted MR image with fat suppression shows multiple nodules in the right lung (arrowheads) representing lung granulomas and a large area of low signal intensity in the left lower lobe (white asterisk) representing air trapping. (**b**) Coronal ventilation map with Fourier decomposition shows region of hypoventilation (black asterisk) in the left lower lobe, matching then area of air trapping on the morphological image. (Courtesy of Dr G Morana, Treviso, Italy)

wall thickening, and bronchiectasis but was inferior to CT for detection of mild bronchial abnormalities [104, 105]. Despite the lower performance for detection of mild disease, MRI should be considered an important alternative to CT in patients with CVID given their increased sensitivity to ionizing radiation [104].

Dynamic Large Airway Disorder

Tracheomalacia

Tracheomalacia is a condition in which the cartilage of the airway becomes soft and losses its normal stiffness. When the intrathoracic pressure increases during normal expira-

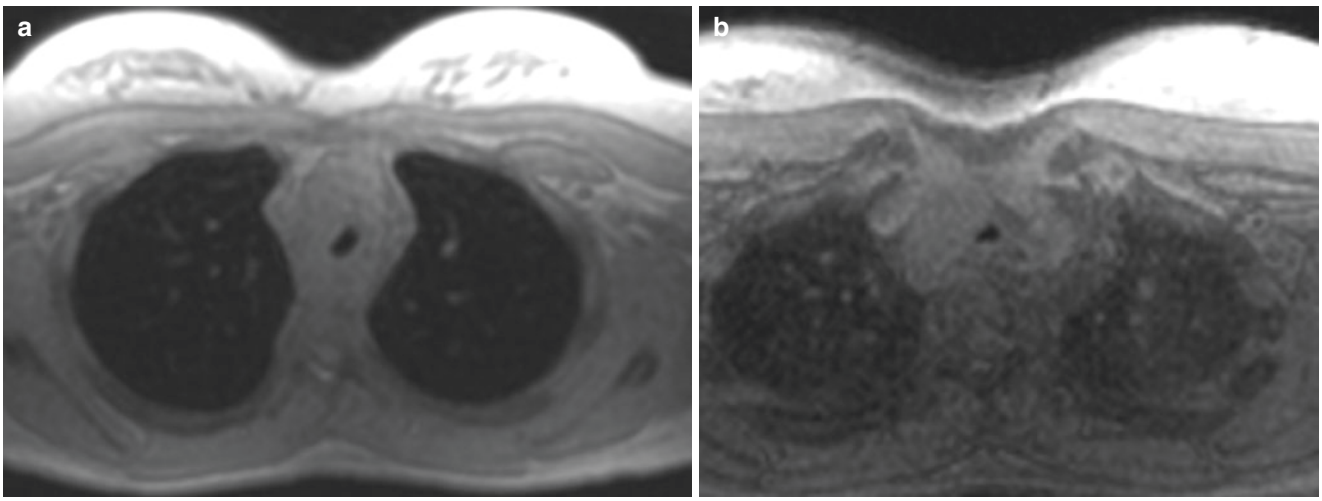

Fig. 21.17 A 8-year-old girl with tracheomalacia. (**a**) Axial 3D SPGR MR image obtained at end-inspiration shows narrowed caliber of the trachea. (**b**) Axial 3D SPGR MR image obtained at end-expiration shows further collapse of the trachea

tion, the weakened cartilage collapses, leading to airway narrowing and obstruction. The airway may be normal in caliber during inspiration when the intrathoracic pressure is negative. Tracheomalacia may be primary, due to intrinsic disorder of cartilage development, or secondary, due to acquired injury to the airway cartilage. The secondary form is more common and causes include trauma, intubation, infection, inflammation, and compression (e.g., by a dilated esophagus in cases of esophageal atresia) [106, 107]. Tracheomalacia is a relatively common cause of respiratory symptoms in children; 15–30% of children undergoing bronchoscopy for respiratory distress are diagnosed with tracheomalacia [108–110].

The gold standard for diagnosis of tracheomalacia is bronchoscopy; however noninvasive imaging is often preferred as a first step in the diagnostic work-up. In addition to being noninvasive, cross-sectional imaging provides the advantage of visualizing extraluminal structures which may be associated with tracheomalacia, such as vascular rings and pulmonary sling. When choosing an imaging test to evaluate tracheomalacia, it is important to consider the dynamic nature of the condition. The airway may appear normal during inspiration; therefore tracheomalacia is often incompletely evaluated on standard radiographs, CT or MRI which are routinely performed at end-inspiration. Therefore, imaging of tracheomalacia requires imaging during both inspiration and expiration or dynamic imaging through the respiratory cycle. Historically, this was achieved with fluoroscopy of the airway during breathing. However, detailed evaluation of the airway is often limited on fluoroscopy, and CT with inspiratory and expiratory image acquisition has become the preferred noninvasive imaging test by many given its ability to evaluate cross-sectional airway diameter and morphology and create 3D/4D reformations [107]. Although image quality is typically excellent with CT, there is concern about radiation exposure, and CT exams require scanning during multiple phases of respiration. This has motivated the development of new MRI techniques that allow dynamic imaging of the airway during breathing [5, 6]. By utilizing an MRI-compatible spirometer that is integrated with the image acquisition, images of the airway and end-inspiration, end-expiration, and cine images throughout the respiratory cycle can be obtained [5, 6]. MR imaging findings of tracheomalacia are similar to findings on CT and include excessive reduction in airway diameter during expiration, which may appear as a "frown" shape or complete collapse [107, 111] (Fig. 21.17). Dynamic spirometer-controlled MRI of the airways is not currently available outside of the research setting, but it is a practical application that may become more widely available in upcoming years.

References

1. Dournes G, Menut F, Macey J, et al. Lung morphology assessment of cystic fibrosis using MRI with ultra-short echo time at submillimeter spatial resolution. Eur Radiol. 2016;26:3811.
2. Ciet P, Tiddens HA, Wielopolski PA, et al. Magnetic resonance imaging in children: common problems and possible solutions for lung and airways imaging. Pediatr Radiol. 2015;45(13):1901–15.
3. Baez JC, Seethamraju RT, Mulkern R, Ciet P, Lee EY. Pediatric chest MR imaging: sedation, techniques, and extracardiac vessels. Magn Reson Imaging Clin N Am. 2015;23(2):321–35.
4. Ciet P, Serra G, Bertolo S, et al. Assessment of CF lung disease using motion corrected PROPELLER MRI: a comparison with CT. Eur Radiol. 2016;26(3):780–7.
5. Ciet P, Wielopolski P, Manniesing R, et al. Spirometer-controlled cine magnetic resonance imaging used to diagnose tracheobronchomalacia in paediatric patients. Eur Respir J. 2014;43(1):115–24.
6. Ciet P, Boiselle PM, Heidinger B, et al. Cine MRI of tracheal dynamics in healthy volunteers and patients with tracheobronchomalacia. AJR Am J Roentgenol. 2017;209(4):757–61.

7. Ciet P, Bertolo S, Ros M, et al. Detection and monitoring of lung inflammation in cystic fibrosis during respiratory tract exacerbation using diffusion-weighted magnetic resonance imaging. Eur Respir J. 2017;50(1):1601437.
8. Bauman G, Puderbach M, Heimann T, et al. Validation of Fourier decomposition MRI with dynamic contrast-enhanced MRI using visual and automated scoring of pulmonary perfusion in young cystic fibrosis patients. Eur J Radiol. 2013;82(12):2371–7.
9. Mithal LB, Patel PS, Mithal D, Palac HL, Rozenfeld MN. Use of gadolinium-based magnetic resonance imaging contrast agents and awareness of brain gadolinium deposition among pediatric providers in North America. Pediatr Radiol. 2017;47(6):657–64.
10. Voskrebenzev A, Gutberlet M, Kaireit TF, Wacker F, Vogel-Claussen J. Low-pass imaging of dynamic acquisitions (LIDA) with a group-oriented registration (GOREG) for proton MR imaging of lung ventilation. Magn Reson Med. 2017;78(4):1496–505.
11. Voskrebenzev A, Gutberlet M, Klimes F, et al. Feasibility of quantitative regional ventilation and perfusion mapping with phase-resolved functional lung (PREFUL) MRI in healthy volunteers and COPD, CTEPH, and CF patients. Magn Reson Med. 2018;79(4):2306–14.
12. Campbell RM Jr. VEPTR: past experience and the future of VEPTR principles. Eur Spine J. 2013;22(Suppl 2):S106–17.
13. Tiddens HA, Stick SM, Wild JM, et al. Respiratory tract exacerbations revisited: ventilation, inflammation, perfusion, and structure (VIPS) monitoring to redefine treatment. Pediatr Pulmonol. 2015;50(Suppl 40):S57–65.
14. Goudar SP, Shah SS, Shirali GS. Echocardiography of coarctation of the aorta, aortic arch hypoplasia, and arch interruption: strategies for evaluation of the aortic arch. Cardiol Young. 2016;26(8):1553–62.
15. Hanneman K, Newman B, Chan F. Congenital variants and anomalies of the aortic arch. Radiographics. 2017;37(1):32–51.
16. Schreiber C, Mazzitelli D, Haehnel JC, Lorenz HP, Meisner H. The interrupted aortic arch: an overview after 20 years of surgical treatment. Eur J Cardiothorac Surg. 1997;12(3):466–9; discussion 469–70.
17. Dillman JR, Yarram SG, D'Amico AR, Hernandez RJ. Interrupted aortic arch: spectrum of MRI findings. AJR Am J Roentgenol. 2008;190(6):1467–74.
18. Yang DH, Goo HW, Seo DM, et al. Multislice CT angiography of interrupted aortic arch. Pediatr Radiol. 2008;38(1):89–100.
19. Bjornard K, Riehle-Colarusso T, Gilboa SM, Correa A. Patterns in the prevalence of congenital heart defects, metropolitan Atlanta, 1978 to 2005. Birth Defects Res A Clin Mol Teratol. 2013;97(2):87–94.
20. Warnes CA. Bicuspid aortic valve and coarctation: two villains part of a diffuse problem. Heart. 2003;89(9):965–6.
21. Dijkema EJ, Leiner T, Grotenhuis HB. Diagnosis, imaging and clinical management of aortic coarctation. Heart. 2017;103(15):1148–55.
22. Backer CL, Monge MC, Popescu AR, Eltayeb OM, Rastatter JC, Rigsby CK. Vascular rings. Semin Pediatr Surg. 2016;25(3):165–75.
23. Backer CL, Mavroudis C, Rigsby CK, Holinger LD. Trends in vascular ring surgery. J Thorac Cardiovasc Surg. 2005;129(6):1339–47.
24. Kellenberger CJ. Aortic arch malformations. Pediatr Radiol. 2010;40(6):876–84.
25. Leonardi B, Secinaro A, Cutrera R, et al. Imaging modalities in children with vascular ring and pulmonary artery sling. Pediatr Pulmonol. 2015;50(8):781–8.
26. Fogel MA, Pawlowski TW, Harris MA, et al. Comparison and usefulness of cardiac magnetic resonance versus computed tomography in infants six months of age or younger with aortic arch anomalies without deep sedation or anesthesia. Am J Cardiol. 2011;108(1):120–5.
27. Dillman JR, Attili AK, Agarwal PP, Dorfman AL, Hernandez RJ, Strouse PJ. Common and uncommon vascular rings and slings: a multi-modality review. Pediatr Radiol. 2011;41(11):1440–54; quiz 1489–1490.
28. Lee KH, Yoon CS, Choe KO, et al. Use of imaging for assessing anatomical relationships of tracheobronchial anomalies associated with left pulmonary artery sling. Pediatr Radiol. 2001;31(4):269–78.
29. Biyyam DR, Chapman T, Ferguson MR, Deutsch G, Dighe MK. Congenital lung abnormalities: embryologic features, prenatal diagnosis, and postnatal radiologic-pathologic correlation. Radiographics. 2010;30(6):1721–38.
30. Berrocal T, Madrid C, Novo S, Gutierrez J, Arjonilla A, Gomez-Leon N. Congenital anomalies of the tracheobronchial tree, lung, and mediastinum: embryology, radiology, and pathology. Radiographics. 2004;24(1):e17.
31. Tilea B, Garel C, Delezoide AL, et al. Prenatal diagnosis of horseshoe lung: contribution of MRI. Pediatr Radiol. 2005;35(10):1010–3.
32. Jeewa A, Culham JA, Human DG. A case of horseshoe lung and complex congenital heart disease in a term newborn. Pediatr Radiol. 2010;40(2):206–9.
33. Hwang HK, Chen MR, Chen SJ, Kao HA, Lee KS, Shih SL. Horseshoe lung with pseudo-ring-sling complex. Pediatr Pulmonol. 2002;34(5):402–4.
34. Festa P, Lamia AA, Murzi B, Bini MR. Tetralogy of fallot with left heart hypoplasia, total anomalous pulmonary venous return, and right lung hypoplasia: role of magnetic resonance imaging. Pediatr Cardiol. 2005;26(4):467–9.
35. Mahani MG, Morani AC, Lu JC, et al. Non-cardiovascular findings in clinical cardiovascular magnetic resonance imaging in children. Pediatr Radiol. 2016;46(4):473–82.
36. Pryce DM. Lower accessory pulmonary artery with intralobar sequestration of lung; a report of seven cases. J Pathol Bacteriol. 1946;58(3):457–67.
37. Lee EY, Dorkin H, Vargas SO. Congenital pulmonary malformations in pediatric patients: review and update on etiology, classification, and imaging findings. Radiol Clin N Am. 2011;49(5):921–48.
38. Lee EY, Boiselle PM, Cleveland RH. Multidetector CT evaluation of congenital lung anomalies. Radiology. 2008;247(3):632–48.
39. Epelman M, Daltro P, Soto G, Ferrari CM, Lee EY. Congenital lung anomalies. In: Coley BD, editor. Caffey's pediatric diagnostic imaging. 12th ed. Philadelphia: Elsevier; 2013. p. 550–66.
40. Epelman M, Kreiger PA, Servaes S, Victoria T, Hellinger JC. Current imaging of prenatally diagnosed congenital lung lesions. Semin Ultrasound CT MR. 2010;31(2):141–57.
41. Eber E. Antenatal diagnosis of congenital thoracic malformations: early surgery, late surgery, or no surgery? Semin Respir Crit Care Med. 2007;28(3):355–66.
42. Laje P, Liechty KW. Postnatal management and outcome of prenatally diagnosed lung lesions. Prenat Diagn. 2008;28(7):612–8.
43. Liszewski MC, Hersman FW, Altes TA, et al. Magnetic resonance imaging of pediatric lung parenchyma, airways, vasculature, ventilation, and perfusion: state of the art. Radiol Clin N Am. 2013;51(4):555–82.
44. Masrani A, McWilliams S, Bhalla S, Woodard PK. Anatomical associations and radiological characteristics of Scimitar syndrome on CT and MR. J Cardiovasc Comput Tomogr. 2018;12:286.
45. Dusenbery SM, Geva T, Seale A, et al. Outcome predictors and implications for management of scimitar syndrome. Am Heart J. 2013;165(5):770–7.
46. Wang H, Kalfa D, Rosenbaum MS, et al. Scimitar syndrome in children and adults: natural history, outcomes, and risk analysis. Ann Thorac Surg. 2018;105(2):592–8.

47. Li J, Thompson TD, Miller JW, Pollack LA, Stewart SL. Cancer incidence among children and adolescents in the United States, 2001–2003. Pediatrics. 2008;121(6):e1470–7.
48. Garey CL, Laituri CA, Valusek PA, St Peter SD, Snyder CL. Management of anterior mediastinal masses in children. Eur J Pediatr Surg. 2011;21(5):310–3.
49. Acker SN, Linton J, Tan GM, et al. A multidisciplinary approach to the management of anterior mediastinal masses in children. J Pediatr Surg. 2015;50(5):875–8.
50. Littooij AS, Kwee TC, Barber I, et al. Whole-body MRI for initial staging of paediatric lymphoma: prospective comparison to an FDG-PET/CT-based reference standard. Eur Radiol. 2014;24(5):1153–65.
51. Hack HA, Wright NB, Wynn RF. The anaesthetic management of children with anterior mediastinal masses. Anaesthesia. 2008;63(8):837–46.
52. Liszewski MC, Ciet P, Sodhi KS, Lee EY. Updates on MRI evaluation of pediatric large airways. AJR Am J Roentgenol. 2017;208(5):971–81.
53. Yalcin B, Demir HA, Tanyel FC, et al. Mediastinal germ cell tumors in childhood. Pediatr Hematol Oncol. 2012;29(7):633–42.
54. Schneider DT, Calaminus G, Koch S, et al. Epidemiologic analysis of 1,442 children and adolescents registered in the German germ cell tumor protocols. Pediatr Blood Cancer. 2004;42(2):169–75.
55. De Backer A, Madern GC, Hakvoort-Cammel FG, Oosterhuis JW, Hazebroek FW. Mediastinal germ cell tumors: clinical aspects and outcomes in 7 children. Eur J Pediatr Surg. 2006;16(5):318–22.
56. Takeda S, Miyoshi S, Ohta M, Minami M, Masaoka A, Matsuda H. Primary germ cell tumors in the mediastinum: a 50-year experience at a single Japanese institution. Cancer. 2003;97(2):367–76.
57. Drevelegas A, Palladas P, Scordalaki A. Mediastinal germ cell tumors: a radiologic-pathologic review. Eur Radiol. 2001;11(10):1925–32.
58. Gaerte SC, Meyer CA, Winer-Muram HT, Tarver RD, Conces DJ Jr. Fat-containing lesions of the chest. Radiographics. 2002;22 Spec No:S61–78.
59. Samuel M, Moore IE, Burge DM. Thoracic wall lipoblastoma: a case report and review of histopathology and cytogenetics. Eur J Pediatr Surg. 2000;10(1):53–7.
60. Ranganath SH, Lee EY, Restrepo R, Eisenberg RL. Mediastinal masses in children. AJR Am J Roentgenol. 2012;198(3):W197–216.
61. Lee EY. Evaluation of non-vascular mediastinal masses in infants and children: an evidence-based practical approach. Pediatr Radiol. 2009;39(Suppl 2):S184–90.
62. de Almeida CPB, Ziegelmann PK, Couban R, Wang L, Busse JW, Silva DR. Predictors of in-hospital mortality among patients with pulmonary tuberculosis: a systematic review and meta-analysis. Sci Rep. 2018;8(1):7230.
63. Lobato MN, Hopewell PC. Mycobacterium tuberculosis infection after travel to or contact with visitors from countries with a high prevalence of tuberculosis. Am J Respir Crit Care Med. 1998;158(6):1871–5.
64. Goussard P, Gie RP, Janson JT, et al. Decompression of enlarged mediastinal lymph nodes due to mycobacterium tuberculosis causing severe airway obstruction in children. Ann Thorac Surg. 2015;99(4):1157–63.
65. Goussard P, Gie R. Airway involvement in pulmonary tuberculosis. Paediatr Respir Rev. 2007;8(2):118–23.
66. Rizzi EB, Schinina V, Cristofaro M, et al. Detection of pulmonary tuberculosis: comparing MR imaging with HRCT. BMC Infect Dis. 2011;11:243.
67. Peprah KO, Andronikou S, Goussard P. Characteristic magnetic resonance imaging low T2 signal intensity of necrotic lung parenchyma in children with pulmonary tuberculosis. J Thorac Imaging. 2012;27(3):171–4.
68. Kleiman MB. Histoplasmosis. In: Cherry JD, Harrison GJ, Kaplan SL, Steinbach WJ, Hotez PJ, editors. Feigin and Cherry's textbook of pediatric infectious diseases. 7th ed. Philadelphia: Elsevier; 2014. p. 2807–32.
69. Cohen MD, Eigen H, Scott PH, et al. Magnetic resonance imaging of inflammatory lung disorders: preliminary studies in children. Pediatr Pulmonol. 1986;2(4):211–7.
70. Chabi ML, Goracci A, Roche N, Paugam A, Lupo A, Revel MP. Pulmonary aspergillosis. Diagn Interv Imaging. 2015;96(5):435–42.
71. Fujimoto K, Meno S, Nishimura H, Hayabuchi N, Hayashi A. Aspergilloma within cavitary lung cancer: MR imaging findings. AJR Am J Roentgenol. 1994;163(3):565–7.
72. Dournes G, Berger P, Refait J, et al. Allergic bronchopulmonary aspergillosis in cystic fibrosis: MR imaging of airway mucus contrasts as a tool for diagnosis. Radiology. 2017;285(1):261–9.
73. Garg MK, Gupta P, Agarwal R, Sodhi KS, Khandelwal N. MRI: a new paradigm in imaging evaluation of allergic bronchopulmonary aspergillosis? Chest. 2015;147(2):e58–9.
74. Blum U, Windfuhr M, Buitrago-Tellez C, Sigmund G, Herbst EW, Langer M. Invasive pulmonary aspergillosis. MRI, CT, and plain radiographic findings and their contribution for early diagnosis. Chest. 1994;106(4):1156–61.
75. Herold CJ, Kramer J, Sertl K, et al. Invasive pulmonary aspergillosis: evaluation with MR imaging. Radiology. 1989;173(3):717–21.
76. MacSweeney F, Papagiannopoulos K, Goldstraw P, Sheppard MN, Corrin B, Nicholson AG. An assessment of the expanded classification of congenital cystic adenomatoid malformations and their relationship to malignant transformation. Am J Surg Pathol. 2003;27(8):1139–46.
77. d'Agostino S, Bonoldi E, Dante S, Meli S, Cappellari F, Musi L. Embryonal rhabdomyosarcoma of the lung arising in cystic adenomatoid malformation: case report and review of the literature. J Pediatr Surg. 1997;32(9):1381–3.
78. Domizio P, Liesner RJ, Dicks-Mireaux C, Risdon RA. Malignant mesenchymoma associated with a congenital lung cyst in a child: case report and review of the literature. Pediatr Pathol. 1990;10(5):785–97.
79. Ozcan C, Celik A, Ural Z, Veral A, Kandiloglu G, Balik E. Primary pulmonary rhabdomyosarcoma arising within cystic adenomatoid malformation: a case report and review of the literature. J Pediatr Surg. 2001;36(7):1062–5.
80. Federici S, Domenichelli V, Tani G, et al. Pleuropulmonary blastoma in congenital cystic adenomatoid malformation: report of a case. Eur J Pediatr Surg. 2001;11(3):196–9.
81. Burge D, Wheeler R. Increasing incidence of detection of congenital lung lesions. Pediatr Pulmonol. 2010;45(1):103; author reply 104.
82. Langston C. New concepts in the pathology of congenital lung malformations. Semin Pediatr Surg. 2003;12(1):17–37.
83. Holder PD, Langston C. Intralobar pulmonary sequestration (a nonentity?). Pediatr Pulmonol. 1986;2(3):147–53.
84. Riedlinger WF, Vargas SO, Jennings RW, et al. Bronchial atresia is common to extralobar sequestration, intralobar sequestration, congenital cystic adenomatoid malformation, and lobar emphysema. Pediatr Dev Pathol. 2006;9(5):361–73.
85. Stocker JT, Madewell JE, Drake RM. Congenital cystic adenomatoid malformation of the lung. Classification and morphologic spectrum. Hum Pathol. 1977;8(2):155–71.
86. Stocker J. The respiratory tract. In: Stocker JT, LP D, editors. Pediatric pathology. 2nd ed. Philadelphia: Lippincott, Williams & Wilkins; 2001. p. 466–73.
87. Alamo L, Gudinchet F, Reinberg O, et al. Prenatal diagnosis of congenital lung malformations. Pediatr Radiol. 2012;42(3):273–83.
88. Esther CR Jr, Barker PM. Pulmonary lymphangiectasia: diagnosis and clinical course. Pediatr Pulmonol. 2004;38(4):308–13.

89. Malone LJ, Fenton LZ, Weinman JP, Anagnost MR, Browne LP. Pediatric lymphangiectasia: an imaging spectrum. Pediatr Radiol. 2015;45(4):562–9.
90. Yao LC, Testini C, Tvorogov D, et al. Pulmonary lymphangiectasia resulting from vascular endothelial growth factor-C overexpression during a critical period. Circ Res. 2014;114(5):806–22.
91. Cleveland RH, Rhein L. Newborn chest. In: Cleveland RH, editor. Imaging in pediatric pulmonology. New York: Springer; 2012. p. 81–97.
92. Chung CJ, Fordham LA, Barker P, Cooper LL. Children with congenital pulmonary lymphangiectasia: after infancy. AJR Am J Roentgenol. 1999;173(6):1583–8.
93. Dodge JA, Lewis PA, Stanton M, Wilsher J. Cystic fibrosis mortality and survival in the UK: 1947–2003. Eur Respir J. 2007;29(3):522–6.
94. Mott LS, Park J, Murray CP, et al. Progression of early structural lung disease in young children with cystic fibrosis assessed using CT. Thorax. 2012;67(6):509–16.
95. Sly PD, Gangell CL, Chen L, et al. Risk factors for bronchiectasis in children with cystic fibrosis. N Engl J Med. 2013;368(21):1963–70.
96. Wielputz MO, Mall MA. Imaging modalities in cystic fibrosis: emerging role of MRI. Curr Opin Pulm Med. 2015;21(6):609–16.
97. Wielputz MO, Eichinger M, Puderbach M. Magnetic resonance imaging of cystic fibrosis lung disease. J Thorac Imaging. 2013;28(3):151–9.
98. Puderbach M, Eichinger M, Gahr J, et al. Proton MRI appearance of cystic fibrosis: comparison to CT. Eur Radiol. 2007;17(3):716–24.
99. Puderbach M, Eichinger M, Haeselbarth J, et al. Assessment of morphological MRI for pulmonary changes in cystic fibrosis (CF) patients: comparison to thin-section CT and chest x-ray. Investig Radiol. 2007;42(10):715–25.
100. Murphy KP, Maher MM, O'Connor OJ. Imaging of cystic fibrosis and pediatric bronchiectasis. AJR Am J Roentgenol. 2016;206(3):448–54.
101. Dournes G, Grodzki D, Macey J, et al. Quiet submillimeter MR imaging of the lung is feasible with a PETRA sequence at 1.5 T. Radiology. 2015;276(1):258–65.
102. Resnick ES, Moshier EL, Godbold JH, Cunningham-Rundles C. Morbidity and mortality in common variable immune deficiency over 4 decades. Blood. 2012;119(7):1650–7.
103. Gathmann B, Mahlaoui N, Gerard L, et al. Clinical picture and treatment of 2212 patients with common variable immunodeficiency. J Allergy Clin Immunol. 2014;134(1):116–26.
104. Arslan S, Poyraz N, Ucar R, Yesildag M, Yesildag A, Caliskaner AZ. Magnetic resonance imaging may be a valuable radiation-free technique for lung pathologies in patients with primary immunodeficiency. J Clin Immunol. 2016;36(1):66–72.
105. Serra G, Milito C, Mitrevski M, et al. Lung MRI as a possible alternative to CT scan for patients with primary immune deficiencies and increased radiosensitivity. Chest. 2011;140(6):1581–9.
106. Carden KA, Boiselle PM, Waltz DA, Ernst A. Tracheomalacia and tracheobronchomalacia in children and adults: an in-depth review. Chest. 2005;127(3):984–1005.
107. Lee EY, Boiselle PM. Tracheobronchomalacia in infants and children: multidetector CT evaluation. Radiology. 2009;252(1):7–22.
108. Jacobs IN, Wetmore RF, Tom LW, Handler SD, Potsic WP. Tracheobronchomalacia in children. Arch Otolaryngol Head Neck Surg. 1994;120(2):154–8.
109. Mair EA, Parsons DS. Pediatric tracheobronchomalacia and major airway collapse. Ann Otol Rhinol Laryngol. 1992;101(4):300–9.
110. Holinger LD. Etiology of stridor in the neonate, infant and child. Ann Otol Rhinol Laryngol. 1980;89(5 Pt 1):397–400.
111. Boiselle PM, Ernst A. Tracheal morphology in patients with tracheomalacia: prevalence of inspiratory lunate and expiratory "frown" shapes. J Thorac Imaging. 2006;21(3):190–6.